SPECIALIZATION PROJECT IN THEORETICAL PHYSICS

Supercurrent transport by Andreev bound states in an external magnetic field

AUTHOR:
Anna Ursula Birkeland BRØYN

SUPERVISOR:
Prof. Jacob LINDER

December 19, 2016

NTNU – Trondheim
Norwegian University of
Science and Technology

Abstract

The supercurrent in the normal region of a superconductor - normal metal - superconductor structure, in an external magnetic field, is studied. The current is found via the energy levels of the Andreev bound states of the system. It is found that a linear vortex pattern occur in the current density when the external field is uniform. The vortex pattern is changed in a predictive manner when the magnetic field is modulated spatially. Interestingly, it was found that certain modulations leave the current unaffected, even for arbitrary large field strengths. Analytical expressions for the precise modulation wavelength producing this phenomenon are derived. Numerical simulations of the system demonstrate that the supercurrent vortex pattern can be spatially controlled via a modulated external field, and could open new perspectives with regard to tailored quantum current distributions.

Preface

This thesis is submitted as a specialization project in quantum condensed matter theory at the Norwegian University of Science and Technology. Its purpose is to gain knowledge in a special field in physics as a preparation for the master thesis. I would like to thank my supervisor Jacob Linder for providing great help and guidance throughout this project and look forward to continue our collaboration.

Anna Brøyn
Trondheim, Norway
December 2016

Contents

Chapter 1

Introduction

In 1911, H. K. Onnes discovered that the electrical resistance in mercury vanished when it was cooled down to a temperature of 4.2 K [1]. This was the first observation of superconductivity and it would go two more decades before W. Meissner and R. Ochsenfeld, in 1933, discovered a second fundamental property of superconductivity, namely the expulsion of magnetic fields below a certain threshold value [2, 3]. The absence of electrical resistance and the expulsion of the magnetic field are macroscopic quantum mechanical effects of which a microscopical description was missing for another two decades. This was finally presented by Bardeen, Cooper and Schieffer in 1957 and is now known as the BCS theory [4]. The theory propose that the supercurrent in a superconductor is transported via pairs of electrons, known as *Cooper pairs*, which condense into an electronic superfluid in which the Cooper pairs can travel without resistance.

When a superconductor (S) is placed in contact with a normal metal (N), Cooper pairs will leak from the superconductor and into the normal metal. This effect is known as the *proximity effect* [5], and allow for superconducting-like properties in materials which originally were non-superconducting. As the Meissner effect expels magnetic fields, superconductivity and magnetism rarely coexists in bulk materials. However, when hybrid structures are exposed to magnetic fields, the proximity effect allows for interplay between superconductivity and magnetism, giving rise to a variety of interesting effects. In recent years new techniques have allowed resolving properties on smaller length scales and lower temperatures, and this has renewed the interest of the subject [6, 7]. There is now a good understanding of many electronic and transport properties of hybrid SN-structures, but there are still many unexplored aspects of the dependency the magnetic field has on those properties.

J. Rowell observed in 1963 that a superconductor-insulator-superconductor structure, exposed to a magnetic field, would have critical current that oscillates in a certain manner, known as Fraunhofer oscillations [8], see figure 1.1(b). It is understood that these oscillations are a consequence

of circulating current vortices (see figure 1.1(a)) which appears in the insulator between the superconductors, due to quantum interference. The vortices are known as Josephson vortices and have later been observed in several SNS-junctions [9, 10], as well as junctions with other materials such as graphene [11–14] and topological insulators [15–18]. They are different from Abrikosov vortices [19], located in the superconductor, which have normal cores and a phase-winding of 2π of the superconducting order parameter.

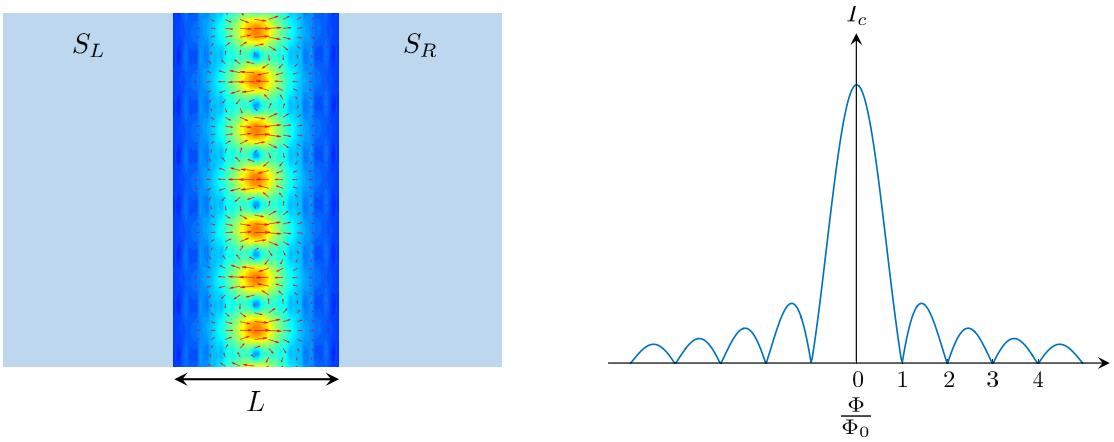

(a) (b)

Figure 1.1: Figure (a) illustrates the supercurrent vortices in the normal region of an SNS-junction when exposed to a uniform magnetic field. The length of the normal region is L while the width is $W \gg L$. Figure (b) shows the Fraunhofer oscillations, with period Φ_0, of the corresponding critical current versus the magnetic flux, Φ.

In wide junctions ($W \gg L$) exposed to a spatially uniform field, research has shown that the vortices are arranged in a chain along the superconducting interface [20–24], like the pattern shown in figure 1.1(a). It is well-known that this pattern is modified by the insulating barriers if $W \simeq L$ [25–27], and in newer research it was found that if the Fermi surface is warped, the vortices are modified into a two-dimensional vortex lattice [28]. In any cases the critical current decays as Fraunhofer oscillations when the field strength is increased, although the decay rate under certain conditions has varied [28, 29]. To our knowledge there has not been any research on the effect a spatially modulated magnetic field has on these properties, and the object of this thesis is to understand how the supercurrent respond to modulated fields and how we can control the vortex pattern and critical current using the magnetic fields.

The outline of the thesis is as follows. In chapter 2 we will give the necessary background theory, explaining the Meissner effect and BCS theory, as well as supercurrent transport theory in hybrid structures. In chapter 3 we define the physical system to consider, namely a two-dimensional SNS-

junction which will be subject to external magnetic fields. In chapter 4 we consider two methods, with different advantages, for deriving the energy levels of the system. These energy levels will in chapter 5 be used to find the current in the junction. In chapter 6 we summarize the results in a conclusion followed by an outlook for future work.

Chapter 2

Superconductivity

2.1 The Meissner effect

Meissner and Ochsenfeld discovered in 1933 [2] that applied magnetic field, H, below some critical limit H_c, would be expelled in the superconductor for temperatures below T_c, resulting in zero field inside the superconductor, $B = \mu_0(H + M) = 0$, so that the magnetization is $M = -H$. Hence, the superconductor is in a sense a perfect diamagnet with susceptibility

$$\chi = \frac{dM}{dH} = -1 \tag{2.1}$$

below the critical temperature T_c. This is called the Meissner effect and is a consequence of induced screening supercurrents at the surface of the superconductor. No current can exist only on the surface of a material as this would imply a finite current in a layer of zero thickness requiring infinite density of free charge. Consequently, the screening current must exist at some finite distance, λ_L, into the superconductor and thus letting the external magnetic field penetrate to a depth λ_L. This penetration depth will depend on the density of superconducting carriers (Cooper pairs) and is a result from the London equations [30] and Ampere's law. On a deeper level, the Meissner effect represents that the photon has become massive inside a superconductor as a result of the spontaneous local U(1) symmetry breaking.

The Meissner effect breaks down as the external field is increased to above the critical limit H_c. Depending on the material we will then get full (in type I superconductors) or partial (in type II superconductors) penetration of magnetic flux and the superconductor will go from the superconducting state into the normal or mixed state, respectively.

2.2 BCS theory

The discovery of the Cooper pairs, which can loosely be thought of as bosonic, was truly remarkable, as it is the key mechanism of superconductivity. There was no known mechanism by which electrons could interact attractively at the time Leon Cooper calculated an effective attractive interaction via a perturbation to the non-interacting Fermi gas. Conventionally they are formed by a phonon-mediated attractive interaction which is overwinning the Coulomb repulsion. However, the exact mechanism of the pairing is not of importance in this thesis, and the following derivation applies for any attractive interaction [1].

2.2.1 The BCS Hamiltonian

The Hamiltonian of the system will consist of two parts, describing the non-interacting and interacting electrons, respectively. A given state is defined by the momentum $\boldsymbol{k}$ and spin σ. In the second quantization formalism the annihilation- and creation operators, $c_{\mathbf{k},\sigma}$ and $c^\dagger_{\mathbf{k},\sigma}$, will destroy and create an electron in the corresponding state, respectively. The number operator $n_{\mathbf{k},\sigma} = c^\dagger_{\mathbf{k},\sigma} c_{\mathbf{k},\sigma}$ counts the number of electrons in the state. The non-interacting part of the Hamiltonian will simply be the energy of each state, $\epsilon_{\boldsymbol{k}} = \hbar^2 k^2/2m$, times the number operator and summed over all states. This will thus be the first term in the Hamiltonian (2.2). The interacting part of the Hamiltonian will describe a scattering process where two electrons in the states ($\boldsymbol{k}$, σ) and ($\boldsymbol{k}'$,σ') are scattered into the states ($\boldsymbol{k}+\boldsymbol{q}$, σ) and ($\boldsymbol{k}'-\boldsymbol{q}$, σ'), i.e. ($\boldsymbol{k}$, σ) and ($\boldsymbol{k}'$, σ') are destroyed by the annihilation operators while ($\boldsymbol{k}+\boldsymbol{q}$, σ) and ($\boldsymbol{k}'-\boldsymbol{q}$, σ') are created by the creation operators. We must also include a matrix element $V_{\boldsymbol{k},\boldsymbol{k}'}$ including both the attractive phonon-mediated interaction and the repulsive Coulomb interaction, between the electrons. The total Hamiltonian including both the non-interacting and the interacting term is thus given as

$$H = \sum_{\mathbf{k},\sigma} \epsilon_{\boldsymbol{k}} c^\dagger_{\mathbf{k},\sigma} c_{\mathbf{k},\sigma} + \sum_{\mathbf{k},\mathbf{k}',\mathbf{q},\sigma,\sigma'} V_{\mathbf{k},\mathbf{k}'}(\mathbf{q},\omega) \mathbf{c}^\dagger_{\mathbf{k}+\mathbf{q},\sigma} \mathbf{c}^\dagger_{\mathbf{k}'-\mathbf{q},\sigma'} \mathbf{c}_{\mathbf{k},\sigma} \mathbf{c}_{\mathbf{k}',\sigma'}. \tag{2.2}$$

We define $\varepsilon_{\boldsymbol{k}} \equiv \epsilon_{\boldsymbol{k}} - \mu$ as the energy above the Fermi surface. The chemical potential, μ, is used in place of the Fermi energy, ϵ_F, as these two quantities are essentially the same in all relevant cases. The attractive interaction will only be valid in a small energy range, ω, above the Fermi-surface, and for electrons on opposite sides of the Fermi-surface. We may therefore let $\boldsymbol{k}' = -\boldsymbol{k}$. Due to the Pauli principle the electrons in the Cooper pairs will in most cases be found in opposite spin states, so we will also let $\sigma' = -\sigma$. By now changing the dummy indices, the Hamiltonian takes the form

$$H - \mu N = \sum_{\mathbf{k},\sigma} \varepsilon_{\boldsymbol{k}} c^\dagger_{\mathbf{k},\sigma} c_{\mathbf{k},\sigma} + \sum_{\boldsymbol{k},\boldsymbol{k}'} V_{\boldsymbol{k},\boldsymbol{k}'} c^\dagger_{\boldsymbol{k},\uparrow} c^\dagger_{-\boldsymbol{k},\downarrow} c_{\boldsymbol{k}',\uparrow} c_{-\boldsymbol{k}',\downarrow}, \tag{2.3}$$

[1] The derivation in this section is inspired by Fossheim and Sudbø 2004, pp. 57-83 [31].

where N is the number of electrons. Henceforth we will write H in place of $H-\mu N$.

2.2.2 Mean field approximation

We will use mean field approximation to simplify the Hamiltonian and assume the fluctuations around the expectation values to be small such that we can write

$$c_{-\mathbf{k},\downarrow}c_{\mathbf{k},\uparrow} = \langle c_{-\mathbf{k},\downarrow}c_{\mathbf{k},\uparrow}\rangle + c_{-\mathbf{k},\downarrow}c_{\mathbf{k},\uparrow} - \langle c_{-\mathbf{k},\downarrow}c_{\mathbf{k},\uparrow}\rangle \equiv \langle c_{-\mathbf{k},\downarrow}c_{\mathbf{k},\uparrow}\rangle + \delta_{\boldsymbol{k}}, \tag{2.4}$$

and only keep $\delta_{\boldsymbol{k}}$ to the first order. By also defining the *gap parameter* as follows

$$\Delta_{\boldsymbol{k}'} = \sum_{\boldsymbol{k}} V_{\boldsymbol{k},\boldsymbol{k}'}\langle c_{-\mathbf{k},\downarrow}c_{\mathbf{k},\uparrow}\rangle, \tag{2.5}$$

the Hamiltonian will simplify to

$$\begin{aligned}
H &= \sum_{\mathbf{k},\sigma}\varepsilon_{\boldsymbol{k}}c^{\dagger}_{\mathbf{k},\sigma}c_{\mathbf{k},\sigma} + \sum_{\boldsymbol{k}}\left[\Delta^{*}_{\boldsymbol{k}}c_{\boldsymbol{k},\uparrow}c_{-\boldsymbol{k},\downarrow} + \Delta_{\boldsymbol{k}}c^{\dagger}_{\boldsymbol{k},\uparrow}c^{\dagger}_{-\boldsymbol{k},\downarrow} - \Delta_{\boldsymbol{k}}\langle c^{\dagger}_{\mathbf{k},\uparrow}c^{\dagger}_{-\mathbf{k},\downarrow}\rangle\right] \\
&= \sum_{\boldsymbol{k}}\left[\varepsilon_{\boldsymbol{k}} - \Delta_{\boldsymbol{k}}\langle c^{\dagger}_{\mathbf{k},\uparrow}c^{\dagger}_{-\mathbf{k},\downarrow}\rangle\right] + \sum_{\boldsymbol{k}}\varepsilon_{\boldsymbol{k}}\left[c^{\dagger}_{\mathbf{k},\uparrow}c_{\mathbf{k},\uparrow} - c_{-\mathbf{k},\downarrow}c^{\dagger}_{-\mathbf{k},\downarrow}\right] + \sum_{\boldsymbol{k}}\left[\Delta^{*}_{\boldsymbol{k}}c_{\boldsymbol{k},\uparrow}c_{-\boldsymbol{k},\downarrow} + \Delta_{\boldsymbol{k}}c^{\dagger}_{\boldsymbol{k},\uparrow}c^{\dagger}_{-\boldsymbol{k},\downarrow}\right] \\
&= E_0 + \sum_{\boldsymbol{k}}\begin{pmatrix}c^{\dagger}_{\mathbf{k},\uparrow} & c_{-\mathbf{k},\downarrow}\end{pmatrix}\begin{pmatrix}\varepsilon_{\boldsymbol{k}} & \Delta_{\boldsymbol{k}} \\ \Delta^{*}_{\boldsymbol{k}} & -\varepsilon_{\boldsymbol{k}}\end{pmatrix}\begin{pmatrix}c_{\mathbf{k},\uparrow} \\ c^{\dagger}_{-\mathbf{k},\downarrow}\end{pmatrix} \\
&\equiv E_0 + \sum_{\boldsymbol{k}}\varphi'^{\dagger}_{\boldsymbol{k}}H'_{\boldsymbol{k}}\varphi'_{\boldsymbol{k}}.
\end{aligned} \tag{2.6}$$

In the above calculations we have used the standard commutation relations for fermions

$$\begin{aligned}
\left[c^{\dagger}_{\mathbf{k},\sigma}, c_{\boldsymbol{k}',\sigma'}\right]_{+} &= \delta_{\boldsymbol{k},\boldsymbol{k}'}\delta_{\sigma,\sigma'} \\
\left[c^{\dagger}_{\mathbf{k},\sigma}, c^{\dagger}_{\boldsymbol{k}',\sigma'}\right]_{+} &= 0 \\
\left[c_{\mathbf{k},\sigma}, c_{\boldsymbol{k}',\sigma'}\right]_{+} &= 0
\end{aligned} \tag{2.7}$$

and defined

$$E_0 \equiv \sum_{\boldsymbol{k}}\left[\varepsilon_{\boldsymbol{k}} - \Delta_{\boldsymbol{k}}\langle c^{\dagger}_{\mathbf{k},\uparrow}c^{\dagger}_{-\mathbf{k},\downarrow}\rangle\right], \quad H'_{\boldsymbol{k}} = \begin{pmatrix}\varepsilon_{\boldsymbol{k}} & \Delta_{\boldsymbol{k}} \\ \Delta^{*}_{\boldsymbol{k}} & -\varepsilon_{\boldsymbol{k}}\end{pmatrix} \quad \text{and} \quad \varphi'_{\boldsymbol{k}} \equiv \begin{pmatrix}c_{\mathbf{k},\uparrow} \\ c^{\dagger}_{-\mathbf{k},\downarrow}\end{pmatrix}.$$

The Hamiltonian (2.6) can be diagonalized by inserting $U_{\boldsymbol{k}}U^{\dagger}_{\boldsymbol{k}} = I$, where I is the identity matrix and U is a unitary matrix:

$$U_{\boldsymbol{k}} = \begin{pmatrix}u_{\boldsymbol{k}} & -v^{*}_{\boldsymbol{k}} \\ v_{\boldsymbol{k}} & u^{*}_{\boldsymbol{k}}\end{pmatrix}, \qquad U^{\dagger}_{\boldsymbol{k}} = \begin{pmatrix}u^{*}_{\boldsymbol{k}} & v^{*}_{\boldsymbol{k}} \\ -v_{\boldsymbol{k}} & u_{\boldsymbol{k}}\end{pmatrix}. \tag{2.8}$$

$u_{\boldsymbol{k}}$ and $v_{\boldsymbol{k}}$ are the coherence factors satisfing the relation $|u_{\boldsymbol{k}}|^2 + |v_{\boldsymbol{k}}|^2 = 1$ and by introducing new variables, α, β and $\theta_{\boldsymbol{k}}$ we can write them as

$$u_{\boldsymbol{k}} = e^{i\alpha}\cos\theta_{\boldsymbol{k}}, \qquad v_{\boldsymbol{k}} = e^{i\beta}\sin\theta_{\boldsymbol{k}}. \tag{2.9}$$

If we now let α, β and $\theta_{\boldsymbol{k}}$ be such that $H_{\boldsymbol{k}} = U_{\boldsymbol{k}}^\dagger H'_{\boldsymbol{k}} U_{\boldsymbol{k}}$ is diagonal, our Hamiltonian will now be on the diagnoal form

$$H = E_0 + \sum_{\boldsymbol{k}} \varphi_{\boldsymbol{k}}^\dagger H_{\boldsymbol{k}} \varphi_{\boldsymbol{k}} \tag{2.10}$$

with $\varphi_{\boldsymbol{k}} \equiv U_{\boldsymbol{k}}^\dagger \varphi'_{\boldsymbol{k}}$:

$$\varphi_{\boldsymbol{k}} \equiv \begin{pmatrix} \gamma_{\boldsymbol{k},\uparrow} \\ \gamma^\dagger_{-\boldsymbol{k},\downarrow} \end{pmatrix} = \begin{pmatrix} u_{\boldsymbol{k}}^* & v_{\boldsymbol{k}}^* \\ -v_{\boldsymbol{k}} & u_{\boldsymbol{k}} \end{pmatrix} \begin{pmatrix} c_{\mathbf{k},\uparrow} \\ c^\dagger_{-\mathbf{k},\downarrow} \end{pmatrix}. \tag{2.11}$$

The new fermionic operators $\gamma_{\boldsymbol{k},\uparrow}$ and $\gamma^\dagger_{-\boldsymbol{k},\downarrow}$ are describing excitations of single quasiparticles.

2.2.3 Diagonalization of the BCS Hamiltonian

We write out the elements of $H_{\boldsymbol{k}}$ in order to find α, β and $\theta_{\boldsymbol{k}}$ that diagonalize the Hamiltonian:

$$\begin{aligned} H_{\boldsymbol{k}} = U_{\boldsymbol{k}}^\dagger H'_{\boldsymbol{k}} U_{\boldsymbol{k}} &= \begin{pmatrix} u_{\boldsymbol{k}}^* & v_{\boldsymbol{k}}^* \\ -v_{\boldsymbol{k}} & u_{\boldsymbol{k}} \end{pmatrix} \begin{pmatrix} \varepsilon_{\boldsymbol{k}} & \Delta_{\boldsymbol{k}} \\ \Delta_{\boldsymbol{k}}^* & -\varepsilon_{\boldsymbol{k}} \end{pmatrix} \begin{pmatrix} u_{\boldsymbol{k}} & -v_{\boldsymbol{k}}^* \\ v_{\boldsymbol{k}} & u_{\boldsymbol{k}}^* \end{pmatrix} \\ &= \begin{pmatrix} \varepsilon_{\boldsymbol{k}}\left(|u_{\boldsymbol{k}}|^2 - |v_{\boldsymbol{k}}|^2\right) + \Delta_{\boldsymbol{k}} u_{\boldsymbol{k}}^* v_{\boldsymbol{k}} + \Delta_{\boldsymbol{k}}^* u_{\boldsymbol{k}} v_{\boldsymbol{k}}^* & \Delta_{\boldsymbol{k}} u_{\boldsymbol{k}}^{*2} - \Delta_{\boldsymbol{k}}^* v_{\boldsymbol{k}}^{*2} - 2\varepsilon_{\boldsymbol{k}} u_{\boldsymbol{k}}^* v_{\boldsymbol{k}}^* \\ \Delta_{\boldsymbol{k}}^* u_{\boldsymbol{k}}^2 - \Delta_{\boldsymbol{k}} v_{\boldsymbol{k}}^2 - 2\varepsilon_{\boldsymbol{k}} u_{\boldsymbol{k}} v_{\boldsymbol{k}} & -\left[\varepsilon_{\boldsymbol{k}}(|u_{\boldsymbol{k}}|^2 - |v_{\boldsymbol{k}}|^2) + \Delta_{\boldsymbol{k}} u_{\boldsymbol{k}}^* v_{\boldsymbol{k}} + \Delta_{\boldsymbol{k}}^* u_{\boldsymbol{k}} v_{\boldsymbol{k}}^*\right] \end{pmatrix}. \end{aligned} \tag{2.12}$$

$u_{\boldsymbol{k}}$ and $v_{\boldsymbol{k}}$ are on the form given in equation (2.9) and we write the gap parameter as $\Delta_{\boldsymbol{k}} = |\Delta_{\boldsymbol{k}}|\, e^{i\varphi}$. As we will see in the following chapters the superconducting phase, φ, plays an extremely important role in hybrid structures such as Josephson junctions. For the off-diagonal elements to be zero we must have $\Delta_{\boldsymbol{k}}^* u_{\boldsymbol{k}}^2 - \Delta_{\boldsymbol{k}} v_{\boldsymbol{k}}^2 - 2\varepsilon_{\boldsymbol{k}} u_{\boldsymbol{k}} v_{\boldsymbol{k}} = 0$. This yields

$$\begin{aligned} 0 &= \Delta_{\boldsymbol{k}}^* u_{\boldsymbol{k}}^2 - \Delta_{\boldsymbol{k}} v_{\boldsymbol{k}}^2 - 2\varepsilon_{\boldsymbol{k}} u_{\boldsymbol{k}} v_{\boldsymbol{k}} \\ &= |\Delta_{\boldsymbol{k}}|\, e^{i(\alpha+\beta)} \cos^2\theta \left(e^{i(\alpha-\beta-\varphi)} - e^{-i(\alpha-\beta-\varphi)} \tan^2\theta_{\boldsymbol{k}} - 2\frac{\varepsilon_{\boldsymbol{k}}}{|\Delta_{\boldsymbol{k}}|} \tan\theta_{\boldsymbol{k}} \right), \end{aligned}$$

such that α, β and $\theta_{\boldsymbol{k}}$ are given by

$$\alpha - \beta = \varphi \qquad \text{and} \qquad \tan\theta_{\boldsymbol{k}} = -\frac{\varepsilon_{\boldsymbol{k}}}{|\Delta_{\boldsymbol{k}}|} \pm \sqrt{\frac{\varepsilon_{\boldsymbol{k}}^2}{|\Delta_{\boldsymbol{k}}|^2} + 1}. \tag{2.13}$$

The resulting coherence factors will thus be

$$u_{\boldsymbol{k}}^2 = \cos^2\theta = \frac{1}{2}\left(1 \pm \frac{\varepsilon_{\boldsymbol{k}}^{\pm}}{\sqrt{\varepsilon_{\boldsymbol{k}}^{\pm 2} + |\Delta_{\boldsymbol{k}}|^2}}\right)$$
$$v_{\boldsymbol{k}}^2 = \sin^2\theta = \frac{1}{2}\left(1 \mp \frac{\varepsilon_{\boldsymbol{k}}^{\pm}}{\sqrt{\varepsilon_{\boldsymbol{k}}^{\pm 2} + |\Delta_{\boldsymbol{k}}|^2}}\right). \tag{2.14}$$

We let $\varepsilon_{\boldsymbol{k}}^{+} > 0$ and $\varepsilon_{\boldsymbol{k}}^{-} < 0$ and notice that we get $u_{\boldsymbol{k}}^2 = 1$ and $v_{\boldsymbol{k}} = 0$ when $\Delta_{\boldsymbol{k}} = 0$, that is in the limit of the normal state when there is no attraction between the electrons, according to equation (2.5). Calculation of the diagonal terms in $H_{\boldsymbol{k}}$ (2.12) yields

$$H_{\boldsymbol{k}} = \begin{pmatrix} E_{\boldsymbol{k}} & 0 \\ 0 & -E_{\boldsymbol{k}} \end{pmatrix} \tag{2.15}$$

where we have defined

$$E_{\boldsymbol{k}} = \sqrt{\varepsilon_{\boldsymbol{k}}^2 + |\Delta_{\boldsymbol{k}}|^2} \tag{2.16}$$

as the quasiparticle excitation energy. It is now clear why $\Delta_{\boldsymbol{k}}$ is refered to as the *gap-parameter* as it gives a gap in the excitation spectrum of the quasiparticles $\varphi_{\boldsymbol{k}}$. This is one of the key result of the derivation. Under the gap there are no allowed single particle states and we understand that the presence of the Cooper pairs has crucial consequences for the single particle density of states. Moreover, we have

$$k^{\pm} = k_F\sqrt{1 + \frac{\varepsilon_{\boldsymbol{k}}^{\pm}}{\mu}} = k_F\sqrt{1 \pm \frac{\sqrt{E_{\boldsymbol{k}}^2 - |\Delta_{\boldsymbol{k}}|^2}}{\mu}} \tag{2.17}$$

where $\mu = \hbar^2 k_F^2/2m$ and $\varepsilon_{\boldsymbol{k}}^{\pm} = \pm\sqrt{E_{\boldsymbol{k}} - |\Delta_{\boldsymbol{k}}|^2}$ is obtained from equation (2.16). We notice how we get a fourfold degeneracy of relevant states, $(k^+, k^-, -k^+, -k^-)$, for each $E_{\boldsymbol{k}}$. The quasiparticle excitation $\gamma_{\boldsymbol{k},\uparrow}^{\dagger}$ in equation (2.11) will be electronlike since we, according to equation (2.14), have $u_{\boldsymbol{k}}^2 \to 1$ and $v_{\boldsymbol{k}}^2 \to 0$ as $\Delta \to 0$ and $c_{\mathbf{k},\uparrow}^{\dagger}$ creates an electron while $c_{-\mathbf{k},\downarrow}$ destroys an electron, leaving a hole. Similarly, $\gamma_{\boldsymbol{k},\uparrow}$ will be holelike. Moreover, from equation (2.17) we see that $\pm k^+$ ($\pm k^-$) corresponds to energy above(below) the Fermi surface and thus $\pm k^+$ ($\pm k^-$) are electron(hole)-like excitations. The direction of the waves is determined from the group velocity,

$$\boldsymbol{v}_g = \frac{1}{\hbar}\frac{\partial E_{\boldsymbol{k}}}{\partial \boldsymbol{k}} = \frac{\varepsilon_{\boldsymbol{k}}^{\pm}}{E_{\boldsymbol{k}}}\frac{\hbar \boldsymbol{k}^{\pm}}{m}, \tag{2.18}$$

and as $\varepsilon_{\boldsymbol{k}}^{-} < 0$ we realize that the holes travel in opposite direction of its wave vector, $\boldsymbol{k}^{-}$.

For convenience we introduce a new variable, η, defined as

$$\eta \equiv \begin{cases} \arccos\left(\frac{E_{\boldsymbol{k}}}{|\Delta_{\boldsymbol{k}}|}\right), & \text{if } E_{\boldsymbol{k}} < |\Delta_{\boldsymbol{k}}| \\ i\,\text{arccosh}\left(\frac{E_{\boldsymbol{k}}}{|\Delta_{\boldsymbol{k}}|}\right), & \text{if } E_{\boldsymbol{k}} > |\Delta_{\boldsymbol{k}}|\,. \end{cases} \tag{2.19}$$

By using this new variable in the expressions for $u_{\boldsymbol{k}}$ and $v_{\boldsymbol{k}}$ in equation (2.14) we find the quantity,

$$\frac{u_{\boldsymbol{k}}}{v_{\boldsymbol{k}}} = e^{i(\eta+\varphi)}, \tag{2.20}$$

which we will find useful in the following chapters.

2.2.4 Bogoliubov-de Gennes equations

In the description above we assumed the Hamiltonian to be position-invariant so that the wave functions could be considered as simple plane waves, $\sim \exp(i\boldsymbol{k}\cdot\boldsymbol{r})$. We took the potential $V(\boldsymbol{r})$ and the vector potential, $\boldsymbol{A}(\boldsymbol{r})$, to be zero and simply replaced the Hamiltonian for a single particle system,

$$h(\boldsymbol{r}) = \frac{1}{2m}\left(\frac{\hbar}{i}\nabla - q\boldsymbol{A}(\boldsymbol{r})\right)^2 - \mu(\boldsymbol{r}) + V(\boldsymbol{r}), \tag{2.21}$$

with $\varepsilon_{\boldsymbol{k}} = \hbar^2 k^2/2m - \mu$. For systems where the momentum is position-dependent we can not do this simplification and introduce instead field operators:

$$\psi(\boldsymbol{r},t) \equiv \sum_{\boldsymbol{k}} U(\boldsymbol{r},t)\varphi_{\boldsymbol{k}}, \qquad \psi^\dagger(\boldsymbol{r},t) \equiv \sum_{\boldsymbol{k}} \varphi^\dagger_{\boldsymbol{k}} U^\dagger(\boldsymbol{r},t). \tag{2.22}$$

The Hamiltonian in equation (2.6) will now be given as

$$H = E_0 + \int d^3r\, \psi^\dagger(\boldsymbol{r},t)\begin{pmatrix} h(\boldsymbol{r}) & \Delta(\boldsymbol{r}) \\ \Delta^*(\boldsymbol{r}) & -h(\boldsymbol{r}) \end{pmatrix}\psi(\boldsymbol{r},t) \equiv E_0 + \int d^3r\, \psi^\dagger(\boldsymbol{r},t) H'(\boldsymbol{r})\psi(\boldsymbol{r},t). \tag{2.23}$$

Again the Hamiltonian may be diagonalized by setting $U^\dagger(\boldsymbol{r},t)H'(\boldsymbol{r})U(\boldsymbol{r},t) = H_{\boldsymbol{k}}$, or equally $H'(\boldsymbol{r})U(\boldsymbol{r},t) = U(\boldsymbol{r},t)H_{\boldsymbol{k}}$, where $H_{\boldsymbol{k}}$ is on the diagonal form in equation (2.15). By separating these equations for each eigenvalue in $H_{\boldsymbol{k}}$ we get the *Bogoliubov de Gennes equations* (BdG equations) [32]:

$$\begin{aligned} \begin{pmatrix} h(\boldsymbol{r}) & \Delta(\boldsymbol{r}) \\ \Delta^*(\boldsymbol{r}) & -h(\boldsymbol{r}) \end{pmatrix}\begin{pmatrix} u(\boldsymbol{r},t) \\ v(\boldsymbol{r},t) \end{pmatrix} &= E_{\boldsymbol{k}}\begin{pmatrix} u(\boldsymbol{r},t) \\ v(\boldsymbol{r},t) \end{pmatrix}, \\ \begin{pmatrix} -h(\boldsymbol{r}) & -\Delta^*(\boldsymbol{r}) \\ -\Delta(\boldsymbol{r}) & h(\boldsymbol{r}) \end{pmatrix}\begin{pmatrix} -v(\boldsymbol{r},t) \\ u(\boldsymbol{r},t) \end{pmatrix} &= E_{\boldsymbol{k}}\begin{pmatrix} -v(\boldsymbol{r},t) \\ u(\boldsymbol{r},t) \end{pmatrix}. \end{aligned} \tag{2.24}$$

The BCS formalism is now generalized to allow for a spatially varying gap parameter $\Delta(\boldsymbol{r}) = \sum_{\boldsymbol{k}} \Delta_{\boldsymbol{k}} e^{i\boldsymbol{k}\cdot\boldsymbol{r}}$.

From equation (2.11) we have $\gamma^{\dagger}_{\boldsymbol{k},\uparrow} = u_{\boldsymbol{k}} c^{\dagger}_{\mathbf{k},\uparrow} + v_{\boldsymbol{k}} c_{-\mathbf{k},\downarrow}$. By letting $u_\sigma(\boldsymbol{r},t)$ and $v_{-\sigma}(\boldsymbol{r},t)$ be the position space representation of $u_{\boldsymbol{k}}$ and $v_{\boldsymbol{k}}$ we can represent $\gamma^{\dagger}_{\boldsymbol{k},\sigma}$ and $\gamma_{\boldsymbol{k},\sigma}$ by the vectors $\Psi_{e,\sigma}$ and $\Psi_{h,\sigma}$, respectively, where Ψ is a vector of the form $\left(u_\uparrow, u_\downarrow, v_\uparrow, v_\downarrow\right)^T$. This gives:

$$\begin{aligned}
\gamma^{\dagger}_{\boldsymbol{k},\uparrow} \rightarrow \Psi_{e,\uparrow} &= \begin{pmatrix} u(\boldsymbol{r},t) \\ 0 \\ 0 \\ v(\boldsymbol{r},t) \end{pmatrix}, \qquad \gamma^{\dagger}_{-\boldsymbol{k},\downarrow} \rightarrow \Psi_{e,\downarrow} = \begin{pmatrix} 0 \\ u(\boldsymbol{r},t) \\ -v(\boldsymbol{r},t) \\ 0 \end{pmatrix}, \\
\gamma_{\boldsymbol{k},\uparrow} \rightarrow \Psi_{h,\uparrow} &= \begin{pmatrix} v^*(\boldsymbol{r},t) \\ 0 \\ 0 \\ u^*(\boldsymbol{r},t) \end{pmatrix}, \qquad \gamma_{-\boldsymbol{k},\downarrow} \rightarrow \Psi_{h,\downarrow} = \begin{pmatrix} 0 \\ -v^*(\boldsymbol{r},t) \\ u^*(\boldsymbol{r},t) \\ 0 \end{pmatrix}.
\end{aligned} \tag{2.25}$$

In order to simplify the notation we define the 2×2-matrices $\hat{H}(\boldsymbol{r}) \equiv \hat{\sigma}_0 h(\boldsymbol{r})$ and $\hat{\Delta}(\boldsymbol{r}) \equiv i\hat{\sigma}_2 \Delta(\boldsymbol{r})$ where $\hat{\sigma}_0$ is the identity matrix and $\hat{\sigma}_i$ with $(i = 1,2,3)$ are the Pauli matrices:

$$\hat{\sigma}_1 = \begin{pmatrix} 0 & 1 \\ 1 & 0 \end{pmatrix} \quad \hat{\sigma}_2 = \begin{pmatrix} 0 & -i \\ i & 0 \end{pmatrix} \quad \hat{\sigma}_3 = \begin{pmatrix} 1 & 0 \\ 0 & -1 \end{pmatrix}. \tag{2.26}$$

Moreover, we define the 2-vectors $\vec{u}(\boldsymbol{r},t) \equiv \left(u_\uparrow(\boldsymbol{r},t) \;\; u_\downarrow(\boldsymbol{r},t)\right)^T$ and $\vec{v}(\boldsymbol{r},t) \equiv \left(v_\uparrow(\boldsymbol{r},t) \;\; v_\downarrow(\boldsymbol{r},t)\right)^T$. The BdG-equations (2.24) can then be written more compact:

$$\begin{pmatrix} \hat{H}(\boldsymbol{r}) & \hat{\Delta}(\boldsymbol{r}) \\ \hat{\Delta}^\dagger(\boldsymbol{r}) & -\hat{H}(\boldsymbol{r}) \end{pmatrix} \begin{pmatrix} \vec{u}(\boldsymbol{r},t) \\ \vec{v}(\boldsymbol{r},t) \end{pmatrix} = E_{\boldsymbol{k}} \begin{pmatrix} \vec{u}(\boldsymbol{r},t) \\ \vec{v}(\boldsymbol{r},t) \end{pmatrix}. \tag{2.27}$$

2.3 Andreev reflection

Andreev reflection is the key mechanism in in the proximity effect which was mentioned in the introduction 1. It describes supercurrent transport in hybrid structures consisting of a normal metal and a superconductor [2]. The complete model was described by Blonder, Tinkham and Klapwijk in 1982 and is now known as the BTK-theory [33].

When an electron with momentum, $\boldsymbol{k}^+ = k_x^+\hat{x} + k_y^+\hat{y} + k_z^+\hat{z}$, and spin, σ, in the normal metal is propagating towards the superconducting interface, it will be scattered with certain probabilities of transmission and reflection. We choose the coordinate system such that the intersection is

[2] The non-superconducting material can be replaced by other materials, but we will in this thesis only consider structures of normal metals and superconductors

placed in the yz-plane, see figure 2.1. There are two possible ways the electron could be transmitted and reflected. The electron may be transmitted into the superconductor as an electron-like quasiparticle, with momentum $\boldsymbol{q}^+ = q_x^+\hat{x} + q_y^+\hat{y} + q_z^+\hat{z}$ and spin σ, or as a hole-like quasiparticle, with momentum $\boldsymbol{q}^- = -q_x^-\hat{x} + q_y^-\hat{y} + q_z^-\hat{z}$ and spin σ. The x-component have negative sign since the wave direction of a hole is opposite of the direction of its wave vector, as explained in section 2.2.3. The electron may be reflected, either in the normal way, i.e. as an electron with momentum, $\boldsymbol{k}_r^+ = -k_x^+\hat{x} + k_y^+\hat{y} + k_z^+\hat{z}$, and the same spin, σ, or by *Andreev reflection* [34]. In Andreev reflection the incoming electron goes into the superconductor and form a Cooper pair with an electron of opposite spin, leaving a reflected hole with momentum $\boldsymbol{k}^- = k_x^-\hat{x} + k_y^-\hat{y} + k_z^-\hat{z}$ and spin $-\sigma$.

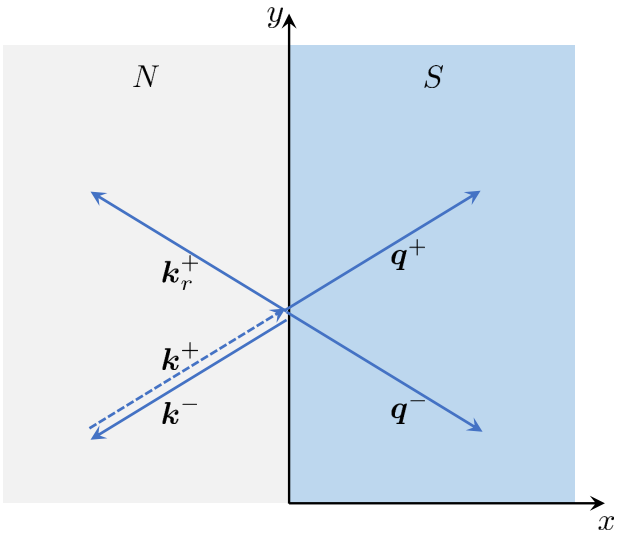

Figure 2.1: A normal metal is in contact with a superconductor. An electron of momentum $\boldsymbol{k}^+$ (dashed line) is either transmitted into the superconductor with momentum $\boldsymbol{q}^+$ (electron-like) or $\boldsymbol{q}^-$ (hole-like), or it is reflected back into the normal metal with momentum $\boldsymbol{k}_r^+$ (electron) or $\boldsymbol{k}^-$ (hole).The arrows indicate the direction of the group velocities (not necessarily the direction of the momentum vectors).

We will in this section ignore the spin degeneracy and write the 4-vector from section 2.2.4 as 2-vectors, $\psi(\boldsymbol{r}) = \begin{pmatrix} u(\boldsymbol{r}) & v(\boldsymbol{r}) \end{pmatrix}^T$. In the simplest case we consider plane waves of the form

$$\psi_{k^+}(\boldsymbol{r}) = \begin{pmatrix} u_0 e^{i\alpha} \\ v_0 e^{i\beta} \end{pmatrix} e^{i\boldsymbol{k}^+\boldsymbol{r}} \quad \text{and} \quad \psi_{k^-}(\boldsymbol{r}) = \begin{pmatrix} v_0 e^{-i\beta} \\ u_0 e^{-i\alpha} \end{pmatrix} e^{i\boldsymbol{k}^-\boldsymbol{r}}, \tag{2.28}$$

with energies $E_{\boldsymbol{k}}$ (2.16) and corresponding wave numbers, $\boldsymbol{k}^{\pm}$, in correspondance with equation (2.25). The incoming, reflected and transmitted wave vectors will in this notation take the form

$$\begin{aligned}
\psi_i(\boldsymbol{r}) &= \begin{pmatrix} 1 \\ 0 \end{pmatrix} e^{i\boldsymbol{k}^+\boldsymbol{r}} \\
\psi_r(\boldsymbol{r}) &= r_{ee}\begin{pmatrix} 1 \\ 0 \end{pmatrix} e^{i\boldsymbol{k}_r^+\boldsymbol{r}} + r_{eh}\begin{pmatrix} 0 \\ 1 \end{pmatrix} e^{i\boldsymbol{k}^-\boldsymbol{r}} \\
\psi_t(\boldsymbol{r}) &= t_{ee}\begin{pmatrix} u_0 e^{i\alpha} \\ v_0 e^{i\beta} \end{pmatrix} e^{i\boldsymbol{q}^+\boldsymbol{r}} + t_{eh}\begin{pmatrix} v_0 e^{-i\beta} \\ u_0 e^{-i\alpha} \end{pmatrix} e^{i\boldsymbol{q}^-\boldsymbol{r}},
\end{aligned} \tag{2.29}$$

where r_{ee}, r_{eh}, t_{ee}, and t_{eh} represent the probabilities of normal reflection, Andreev reflection, electron-like transmission and hole-like transmission, respectively. The Andreev reflection is retro reflective [35, 36] and the hole will move along the same path as the incoming electron as illustrated in figure 2.1. In the opposite situation in which an inomiing hole is Andreev reflected into an electron, a Cooper pair is "dragged" from the superconductor and into the normal metal. This illustrates how the Andreev reflection is the mechanism behind the proximity effect.

In equation (2.16) we found that only energies above the energy gap, Δ, are allowed for the quasiparticles. Consequently, when $E_{\boldsymbol{k}} < \Delta$ the amplitudes t_{ee} and e_{eh} will be zero and only reflection (either normal or Andreev reflection) is allowed. If there is no barrier at the interface, there will be no normal reflection and only Andreev reflection will be allowed. States with such energies in SNS-junctions would thus be trapped in the normal metal by the Andreev reflections and are referred to as Andreev bound states (ABS).

2.4 Josephson current

A Josephson junction is a device consisting of two superconductors that is brought into contact via a *weak link*, in which the *critical current* is much lower than in the bulk superconductor. In the SNS-junction the normal metal plays the role as the weak link. The critical current is the maximum supercurrent that can exist in the structure and is related to the density of Cooper pairs. The proximity effect allows for leakage of Cooper pairs into the normal metal, but the density of Cooper pairs will be much lower than in the bulk superconductor, and consequently so will the critical current. Brian D. Josephson predicted in 1962 that supercurrents would flow through the junction even without any applied voltage [37]. Instead, the current was driven by a difference in the superconducting phase, φ, between the two superconductors. We will in this section derive the Josephson current and how it is related to the free energy of the system.

The number operator, N, of the Cooper pairs in the superconductor, and the superconducting

phase φ are canonical conjugate variables [38]:

$$\hbar\dot{N} = -\frac{\partial H}{\partial \varphi} \qquad \hbar\dot{\varphi} = \frac{\partial H}{\partial N}. \tag{2.30}$$

The tunneling current through a weak link from a superconductor S_L with number of Cooper pairs N_L to a superconductor S_R of N_R Cooper pairs will be given as

$$I = q\dot{N}_L = -q\dot{N}_R \tag{2.31}$$

where $q = -2e$ is the charge of a Cooper pair. Combining equation (2.30) and (2.31) yields

$$I = \frac{2e}{\hbar}\frac{\partial H}{\partial \varphi_L} = -\frac{2e}{\hbar}\frac{\partial H}{\partial \varphi_R}. \tag{2.32}$$

We define the phase difference $\Delta\varphi = \varphi_L - \varphi_R$, and as only this quantity (not the individual phases) has physical meaning, we let $\partial\varphi_L \to \partial\Delta\varphi$ and $\partial\varphi_R \to -\partial\Delta\varphi$. Hence

$$I = \frac{2e}{\hbar}\frac{\partial H}{\partial(\Delta\varphi)}. \tag{2.33}$$

Taking the expectation value of this gives the Josephson current in terms of the free energy, F

$$\langle I\rangle = \frac{2e}{\hbar}\frac{\partial F}{\partial(\Delta\varphi)}, \tag{2.34}$$

since

$$\frac{\partial F}{\partial(\Delta\varphi)} = -\frac{1}{\beta}\frac{1}{Z}\frac{\partial Z}{\partial(\Delta\varphi)} = -\frac{1}{\beta Z}\mathrm{Tr}\left[-\beta\frac{\partial H}{\partial(\Delta\varphi)}e^{-\beta H}\right] = \frac{1}{Z}\mathrm{Tr}\left[\frac{\partial H}{\partial(\Delta\varphi)}e^{-\beta H}\right] = \left\langle\frac{\partial H}{\partial(\Delta\varphi)}\right\rangle \tag{2.35}$$

with Z as the partition function:

$$Z = e^{-\beta F} = \mathrm{Tr}\left[e^{-\beta H}\right] \tag{2.36}$$

and $\beta = 1/k_B T$. As we find the derivative of the phase difference, $\Delta\varphi$, in the expression for the Josephson current, we realize that the current is *phase*-driven. These predictions have been confirmed experimentally for a large number of systems [39–41]. As we will see in the following chapters the superconducting phase is a driving mechanism of the Josephson current on equal footing with the vector potential in a magnetic field.

2.5 Free energy

In order to relate the Josephson current to the energy levels, $E_{\boldsymbol{k}}$, we will here derive the free energy, F, in terms of the energy levels of the superconducting system. The diagonal Hamiltonian in

equation (2.10) is on the form of a free fermion gas:

$$\begin{aligned} H &= E_0 + \sum_{\boldsymbol{k}} \begin{pmatrix} \gamma^\dagger_{\boldsymbol{k},\uparrow} & \gamma_{-\boldsymbol{k},\downarrow} \end{pmatrix} \begin{pmatrix} E_{\boldsymbol{k}} & 0 \\ 0 & -E_{\boldsymbol{k}} \end{pmatrix} \begin{pmatrix} \gamma_{\boldsymbol{k},\uparrow} \\ \gamma^\dagger_{-\boldsymbol{k},\downarrow} \end{pmatrix} \\ &= E_0 + \sum_{\boldsymbol{k}} \left[E_{\boldsymbol{k}} \gamma^\dagger_{\boldsymbol{k},\uparrow} \gamma_{\boldsymbol{k},\uparrow} - E_{\boldsymbol{k}} \left(1 - \gamma^\dagger_{-\boldsymbol{k},\downarrow} \gamma_{-\boldsymbol{k},\downarrow} \right) \right] \\ &= E_0 + \sum_{\boldsymbol{k}} E_{\boldsymbol{k}} \left(N_\uparrow + N_\downarrow - 1 \right) \end{aligned} \tag{2.37}$$

where $N_\uparrow$ and $N_\downarrow$ denotes the number of single particles of respective spin up and down in each state $\boldsymbol{k}$. We find the partition function of the system using the Pauli exclusion principle of fermions such that $N_\uparrow$ and $N_\downarrow$ can take the values 0 or 1. Hence, partition function is

$$\begin{aligned} Z &= \sum e^{-\beta H} = e^{-\beta E_0} \sum_{N_\uparrow, N_\downarrow} e^{-\beta \sum_k E_{\boldsymbol{k}} (N_\uparrow + N_\downarrow - 1)} = e^{-\beta E_0} \prod_{\boldsymbol{k}} e^{\beta E_{\boldsymbol{k}}} \sum_{N_\uparrow} e^{-\beta E_{\boldsymbol{k}} N_\uparrow} \sum_{N_\downarrow} e^{-\beta E_{\boldsymbol{k}} N_\downarrow} \\ &= e^{-\beta E_0} \prod_{\boldsymbol{k}} e^{\beta E_{\boldsymbol{k}}} \left(1 + e^{-\beta E_{\boldsymbol{k}}} \right)^2 = e^{-\beta E_0} \prod_{\boldsymbol{k}} \left(2 \cosh \left(\frac{\beta E_{\boldsymbol{k}}}{2} \right) \right)^2 . \end{aligned} \tag{2.38}$$

We can now easily use the relation between the partition function and the free energy to obtain the free energy in terms of the energy levels, $E_{\boldsymbol{k}}$:

$$F = -\frac{1}{\beta} \ln(Z) = E_0 - 2 k_B T \sum_{\boldsymbol{k}} \ln \left[2 \cosh \left(\frac{E_{\boldsymbol{k}}}{2 k_B T} \right) \right] . \tag{2.39}$$

In chapter 4 we will find the energy levels of selected systems and by using this expression for the free energy along with the Josephson current (2.34), we will be able to find the supercurrent in the systems.

Chapter 3

Physical system

We will in the following chapters consider a two-dimensional SNS-junction, of length L and width W, placed in the xy-plane, with the interfaces parallel to the y-axis at $x = -L/2$ and $x = L/2$, see figure 3.1. The quasiparticle waves are represented by the four-component vectors $\Psi(x,y) = \begin{pmatrix}\vec{u}(x,y) & \vec{v}(x,y)\end{pmatrix}^T$ as used in the Bogoliubov equations (2.27) and we let the gap parameter, $\Delta(x)$, be position-independent in each superconductor. Moreover, the material in each superconductor is assumed to be the same such that the magnitude of Δ is equal in left and right superconductor. However, we allow the gap parameter to have different phases, φ_L and φ_R, in the left and right superconductor, respectively, such that the superconducting phase difference between the two superconductors is $\Delta\varphi = \varphi_L - \varphi_R$. Necessarily, the gap parameter is zero in the normal metal and the overall gap parameter is

$$\Delta(x) = \Delta\left(e^{i\phi_L}\Theta(-L/2-x) + e^{i\phi_R}\Theta(x-L/2)\right), \tag{3.1}$$

where $\Theta(x)$ is the Heaviside step function. The Hamiltonian will be on the form given in equation (2.21). We allow for different chemical potential, μ_S and μ_N, but assume the effective mass to be equal in all regions, i.e. $m_S = m_N \equiv m$. Moreover, we let $V(x)$ be a delta-potential barrier at the interfaces and allow for different strengths, i.e. $V(x) = V_L\delta(x+L/2) + V_R\delta(x-L/2)$. The overall Hamiltonian is

$$h(x,y) = h_S(x,y)\left[\Theta(-L/2-x) + \Theta(x-L/2)\right] + h_N(x,y)\Theta(x+L/2)\Theta(L/2-x) + V_L\delta(x) + V_R\delta(x-L) \tag{3.2}$$

where the Hamiltonian in the superconductors (S) and normal metal (N) is given as

$$h_{S/N}(x,y) = \frac{1}{2m}\left(-i\hbar\nabla - q\boldsymbol{A}(x,y)\right)^2 - \mu_{S/N} \tag{3.3}$$

and $\boldsymbol{A}$ is the vector potential allowing for an external magnetic field $\boldsymbol{B} = \nabla \times \boldsymbol{A}$.

For the analytical calculations we will consider the semiclassical limit $k_F L \gg 1$, in which the Andreev bound states can be associated with classical trajectories, as illustrated in figure 3.1. These trajectories can be thought of as single-mode waveguides connecting the two superconductors. We will consider a circular Fermi surface with isotropic dependence on the wave vector $\boldsymbol{k} = (k_x, k_y) = (k_F \cos\theta_k, k_F \sin\theta_k)$ and work in the short-junction regime $L \ll \xi$, with $\xi = \hbar v_f / \Delta$ being the superconducting coherence length induced by the proximity effect [28].

In the preceding chapters we will look at three different situations. First, in section 4.1 and 5.1, we will consider the system without external field or barriers at the interfaces. Next, in section 4.2 and 5.2, we will include the barriers at each interface, but keep the external field turned off. Finally, in section 4.3 and 5.3, we will include an external field, and take the barriers to be transparent. The situations without the external field is well known [31] and will be used for comparison. There has also been research on the junction in a uniform external magnetic field, both for one-dimensional and two-dimensional systems [20–28]. However, we will here also consider modulated magnetic fields, which to the extend of our knowledge have not yet been explored. Our strategy in all three situations is to first find the ABS-energies (chapter 4) and use this result to find the Josephson current (chapter 5).

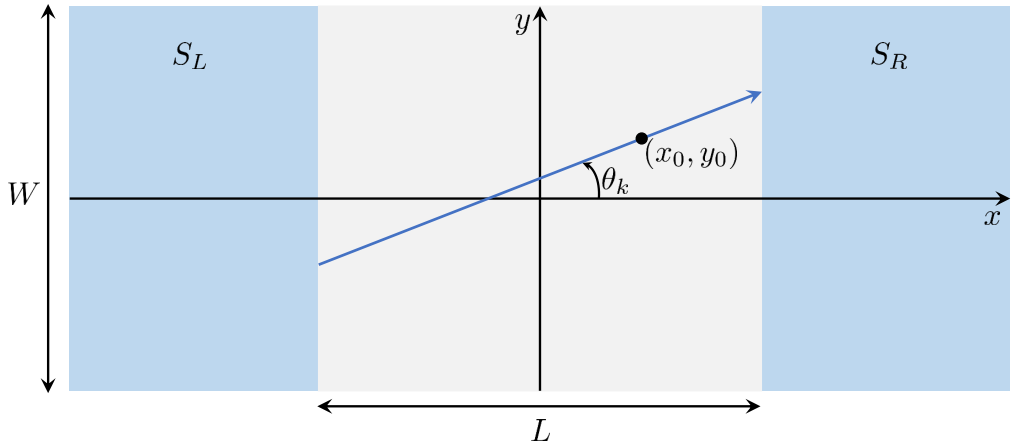

Figure 3.1: A Josephson junction formed by two superconductors of phase difference $\Delta\varphi$ connected by a normal metal of length L and width W. An electron trajectory used for semiclassical calculations of the supercurrent density at (x_0, y_0) is indicated.

Chapter 4

Andreev bound state energies in an SNS-junction

We will in this chapter find the ABS energies in the three situations described in chapter 3. For the situations without barriers the Andreev bound states will accumulate phase shifts as it travels along the classical trajectory, described in chapter 3, and as it is Andreev reflected at the interfaces. This allow us to use the Bohr-Sommmerfeld quantization condition [42] to find the ABS energies. When we include barriers the Andreev reflections can not be expressed as simple phase shifts and we must find the energies by setting up the wave-functions in each region and use boundary conditions to solve the system. The main focus in this thesis is on the situation with external magnetic field, and the motivation behind section 4.2 is just as much to present an alternative approach for finding the energy levels as it is to find the current in the system with barriers. Although the quantization approach is simpler to use it has limitations and is thus not applicable in all systems, such as systems with interface barriers. In future work it could be relevant to include both barriers and magnetic field and the limitations of the quantization condition force us to use alternative approaches such as the one presented in section 4.2.

4.1 ABS energies without barriers or applied field

We will first consider the system with no applied field ($\boldsymbol{A} = 0$) and no barriers ($V_L = V_R = 0$). In section 4.1.1 we use the theory from section 2.3 to find the phase shift accumulated over a penetration depth in the superconductor when an electron or a hole is Andreev reflected at the superconducting interface. This will next be added to the phase accumulated when the electron or hole is traveling along the trajectory in figure 3.1. The total phase shift of the Andreev bound state is used in the Bohr-Sommerfled quantization condition from which the energies are found.

4.1.1 Andreev reflection amplitude

The probability amplitudes from section 2.3 may be found by using the boundary conditions at the interface between the normal metal and the superconductor. With no barriers the boundary conditions yields

$$\begin{aligned} \psi_i(0,y) + \psi_r(0,y) &= \psi_t(0,y) \\ \frac{\partial}{\partial x}\psi_i(0,y) + \frac{\partial}{\partial x}\psi_r(0,y) &= \frac{\partial}{\partial x}\psi_t(0,y). \end{aligned} \tag{4.1}$$

We insert the wave functions, given in equation (2.29), in the boundary conditions and solve the system. The resulting amplitudes are given as

$$\begin{aligned} r_{eh} &= \frac{2e^{-i\varphi}}{\frac{u_0}{v_0}\frac{k_x^- + q^-}{k_x^+ + k_x^-}\left(1 + \frac{k_x^+}{q_x^+}\right) + \frac{v_0}{u_0}\frac{k_x^+ - q_x^-}{k_x^+ + k_x^-}\left(1 - \frac{k_x^-}{k_x^+}\right)} \\ r_{ee} &= \left(\frac{u_0}{v_0}\frac{k_x^+ + q^-}{k_x^+ + k_x^-} + \frac{v_0}{u_0}\frac{k_x^+ - q^-}{k_x^+ + k_x^-}\right) e^{i\varphi} r_{eh} \\ t_{ee} &= \frac{1}{v_0}\frac{k_x^- + q_x^-}{k_x^+ + k_x^-} e^{-i\beta} r_{eh} \\ t_{eh} &= \frac{1}{u_0}\frac{k_x^+ - q_x^-}{k_x^+ + k_x^-} e^{i\alpha} r_{eh}, \end{aligned} \tag{4.2}$$

where $\varphi = \alpha - \beta$ is the phase of the gap parameter as shown in section 2.2.3. The Andreev reflection amplitude, r_{eh}, may be simplified in the Andreev approximation [34] in which we let $k_x^\pm \approx q_x^\pm$:

$$r_{eh} = \frac{v_0}{u_0} e^{-i\varphi} \equiv e^{-i\eta} e^{-i\varphi}, \tag{4.3}$$

where η is as defined in equation (2.19). Similarly, the amplitude of an incoming hole which is Andreev reflected as an electron will be:

$$r_{he} = \frac{v_0}{u_0} e^{i\varphi} = e^{-i\eta} e^{i\varphi}. \tag{4.4}$$

Hence, the Andreev reflection give a phase shift of $-\eta \mp \varphi$, where we use the upper (lower) sign if the incoming particle is an electron (hole) .

4.1.2 Bohr-Sommerfeld quantization

In the short junction regime, the continuous quasiparticle excitation spectrum ($E_{\boldsymbol{k}} > \Delta$) will not contribute to the Josephson current [43] and it is sufficient to restrict our selves to energies below the gap $E_{\boldsymbol{k}} < \Delta$ which yields $\eta = \arccos(E_{\boldsymbol{k}}/\Delta)$, according to equation(2.19). The Bohr-Sommerfeld

quantization condition require the total phase obtained by the state in a whole cycle to be a multiple of 2π [42]. An electron starting at the left interface traveling in the xy-plane towards the right interface along a trajectory at an angle θ (see figure 3.1) would gain a phase of $L(k_x^+ + k_y^+ \tan\theta)$, before it is Andreev reflected at the right interface with the amplitude r_{eh} and thus gaining a phase of $-\eta - \varphi_R$. The state would then continue as a hole traveling back along the same trajectory, accumulating a phase of $-L(k_x^- + k_y^- \tan\theta)$, before it is Andreev reflected back to its original state. The total phase in the quantization condition is then

$$\begin{aligned} 2\pi n = \oint d\phi &= \int_L^R \pm\boldsymbol{k}^{\pm} \cdot d\boldsymbol{l} + \phi^R_{(eh)(he)} + \int_R^L \pm\boldsymbol{k}^{\mp} \cdot d\boldsymbol{l} + \phi^L_{(he)(eh)} \\ &= L(k_x^+ - k_x^-) + L\tan\theta(k_y^+ - k_y^-) - 2\eta \pm \Delta\varphi \end{aligned} \tag{4.5}$$

where $\phi^{R/L}_{(eh)(he)} = -\eta \mp \varphi_{R/L}$ is the phase from Andreev reflection of an electron (hole). The upper sign indicate that the state starts out as a right-going electron, while the lower sign indicate that it starts as a right-going hole. Again we use the Andreev approximation and let $k_x^+ \approx k_x^-$ and $k_y^+ \approx k_y^-$ such that the two first terms vanish and the quantization condition is simply

$$2\pi n = -2\eta \pm \Delta\varphi. \tag{4.6}$$

4.1.3 ABS energy

By inserting η from equation (2.19) in the quantization condition above (4.6) we find the Andreev energy levels

$$E_{\boldsymbol{k}} = \Delta\cos\eta = \Delta\cos\left(\frac{\Delta\varphi}{2}\right). \tag{4.7}$$

This is the well known result in an SNS Josephson junction [44].

4.2 ABS energies with barriers

We will now allow for barriers at the superconducting interfaces. Then the Andreev reflection amplitude will be more complicated so that we can not express it as a phase shift like we did above and the quantization condition is not applicable. We will instead find the energies by setting up the wave-functions in each region, insert the wave-functions in the boundary conditions and solve the system of equations. The Hamiltonian in each region will be as given in equation (3.3), but with no external field so that we can set $\boldsymbol{A}$ to zero. Hence, the Hamiltonian is

$$h_{S/N}(x,y) = -\hbar^2\nabla^2/2m - \mu_{S/N}. \tag{4.8}$$

4.2.1 Boundary conditions

We start by finding the boundary conditions at the superconducting interfaces. Charge conservation yields continuous wave-functions at the interfaces:

$$\begin{aligned}\Psi_L(-L/2,y) &= \Psi_N(-L/2,y) \equiv \Psi(-L/2,y),\\ \Psi_R(L/2,y) &= \Psi_N(L/2,y) \equiv \Psi(L/2,y),\end{aligned} \tag{4.9}$$

but due to the delta potentials at the interfaces we will find the derivative to be discontinuous. We find the boundary conditions for the derivatives at the left interface by integrating the BdG-equations (2.27) over a small distance ϵ around $x=-L/2$ and then let $\epsilon\to 0$:

$$\begin{aligned}
0 &= \lim_{\epsilon\to 0}\int_{-L/2-\epsilon}^{-L/2+\epsilon} E_{\boldsymbol{k}}\Psi(x,y)dx = \lim_{\epsilon\to 0}\int_{-L/2-\epsilon}^{-L/2+\epsilon}\begin{pmatrix}\hat{H}(x,y) & \hat{\Delta}(x)\\ \hat{\Delta}^\dagger(x) & -\hat{H}(x,y)\end{pmatrix}\Psi(x,y)dx\\
&= \lim_{\epsilon\to 0}\int_{-L/2-\epsilon}^{-L/2^-}\begin{pmatrix}h_S(x,y)\hat{\sigma}_0 & i\Delta(x)\hat{\sigma}_2\\ -i\Delta^*(x)\hat{\sigma}_2 & -h_S(x,y)\hat{\sigma}_0\end{pmatrix}\Psi_L(x,y)dx + \begin{pmatrix}V_L\hat{\sigma}_0 & 0\\ 0 & -V_L\hat{\sigma}_0\end{pmatrix}\Psi(-L/2,y)\\
&\quad + \lim_{\epsilon\to 0}\int_{-L/2^+}^{-L/2+\epsilon}\begin{pmatrix}h_N(x)\hat{\sigma}_0 & 0\\ 0 & -h_S(x)\hat{\sigma}_0\end{pmatrix}\Psi_N(x,y)dx\\
&= \begin{pmatrix}\hat{\sigma}_0 & 0\\ 0 & -\hat{\sigma}_0\end{pmatrix}\left(V_L\Psi(-L/2,y) - \frac{\hbar^2}{2m}\lim_{\epsilon\to 0}\left(\int_{-L/2-\epsilon}^{-L/2^-}\frac{\partial^2}{\partial x^2}\Psi_L(x,y)dx + \int_{-L/2^+}^{-L/2+\epsilon}\frac{\partial^2}{\partial x^2}\Psi_N(x,y)dx\right)\right)\\
&= \begin{pmatrix}\hat{\sigma}_0 & 0\\ 0 & -\hat{\sigma}_0\end{pmatrix}\left(V_L\Psi(-L/2,y) - \frac{\hbar^2}{2m}\left(\frac{\partial\Psi_N}{\partial x}\Big|_{x=-L/2} - \frac{\partial\Psi_L}{\partial x}\Big|_{x=-L/2}\right)\right).
\end{aligned}$$

Hence, the boundary condition at the left interface for the derivatives is

$$\frac{\partial\Psi_N}{\partial x}\Big|_{x=-L/2} - \frac{\partial\Psi_L}{\partial x}\Big|_{x=-L/2} = \frac{2m}{\hbar^2}V_L\Psi(-L/2,y). \tag{4.10}$$

and by similar calculations we find

$$\frac{\partial\Psi_R}{\partial x}\Big|_{x=L/2} - \frac{\partial\Psi_N}{\partial x}\Big|_{x=L/2} = \frac{2m}{\hbar^2}V_R\Psi(L/2,y). \tag{4.11}$$

as boundary condition at the right interface.

4.2.2 Wave functions in the superconduction region

We will now identify the wavefunctions in each region, starting with the superconductors. The solution of the BdG-equations (2.27) that satisfy the boundary conditions found above will be on the form

$$\Psi_{\boldsymbol{k}^\pm}(\boldsymbol{r}) = \begin{pmatrix}\vec{u}_{\boldsymbol{k}}\\ \vec{v}_{\boldsymbol{k}}\end{pmatrix}e^{i\boldsymbol{k}^\pm\cdot\boldsymbol{r}}. \tag{4.12}$$

Inserting the wavefunctions of this form in the time-independent Schrödinger equation yields

$$h(\boldsymbol{r})\Psi_{\boldsymbol{k}^\pm}(\boldsymbol{r}) = \left(\frac{\hbar^2 k^{\pm 2}}{2m} - \mu\right)\Psi_{\boldsymbol{k}^\pm}(\boldsymbol{r}) \equiv \varepsilon_k^\pm \Psi_{\boldsymbol{k}^\pm}(\boldsymbol{r}), \tag{4.13}$$

where we let $h(\boldsymbol{r}) = h_S(x,y)$ be as given in (4.8) in the superconducting region. The eigenvalue problem in the BdG-equations (2.27) has non-trivial solutions if the energies, $E_{\boldsymbol{k}}$ satisfy

$$\begin{aligned} 0 &= \det\begin{pmatrix} \left(\varepsilon_{\boldsymbol{k}}^\pm - E_{\boldsymbol{k}}\right)\hat{\sigma}_0 & i\Delta\hat{\sigma}_2 \\ -i\Delta^*\hat{\sigma}_2 & \left(-\varepsilon_{\boldsymbol{k}}^\pm - E_{\boldsymbol{k}}\right)\hat{\sigma}_0 \end{pmatrix} \\ &= \left(\varepsilon_{\boldsymbol{k}}^\pm - E_{\boldsymbol{k}}\right)^2 \left(\varepsilon_{\boldsymbol{k}}^\pm + E_{\boldsymbol{k}} + \frac{\Delta^2}{\varepsilon_{\boldsymbol{k}}^\pm - E_{\boldsymbol{k}}}\right)^2. \end{aligned} \tag{4.14}$$

As $E_{\boldsymbol{k}} = \varepsilon_{\boldsymbol{k}}^\pm$ would give zero in the denominator when Δ is non-zero, the only solution to the above equation (4.14) is

$$E_{\boldsymbol{k}}^2 = \varepsilon_{\boldsymbol{k}}^{\pm 2} + \Delta^2 \tag{4.15}$$

in correspondence with the energies obtained in equation (2.16). We will only consider positive energies, $E_{\boldsymbol{k}} = \sqrt{\varepsilon_{\boldsymbol{k}}^{\pm 2} + \Delta^2}$, and $k^\pm$ and $\varepsilon_{\boldsymbol{k}}^\pm$ will be as in equation (2.17). Electronlike quasiparticles will have $\varepsilon_{\boldsymbol{k}}^+ = +\sqrt{E_{\boldsymbol{k}}^2 - \Delta^2} = i\Delta\sin\eta$ for which we find the (non-normalized) wave-functions

$$\Psi_{e,\uparrow}^\pm(x,y) = \begin{pmatrix} e^{i(\eta+\varphi)} \\ 0 \\ 0 \\ 1 \end{pmatrix} e^{i(\pm k_x^+ x + k_y^+ y)} \quad \text{and} \quad \Psi_{e,\downarrow}^\pm(x,y) = \begin{pmatrix} 0 \\ e^{i(\eta+\varphi)} \\ -1 \\ 0 \end{pmatrix} e^{i(\pm k_x^+ x + k_y^+ y)}, \tag{4.16}$$

where $\Psi_{e,\sigma}^+$ are right-going waves, while $\Psi_{e,\sigma}^-$ are left-going waves. Similarly, for $\varepsilon_k^- = -\sqrt{E_k^2 - \Delta^2} = -i\Delta\sin\eta$ we get the wave-functions describing holelike quasiparticles:

$$\Psi_{h,\uparrow}^\pm(x,y) = \begin{pmatrix} 1 \\ 0 \\ 0 \\ e^{i(\eta-\varphi)} \end{pmatrix} e^{i(\pm k_x^- x + k_y^- y)} \quad \text{and} \quad \Psi_{h,\downarrow}^\pm(x,y) = \begin{pmatrix} 0 \\ -1 \\ e^{i(\eta-\varphi)} \\ 0 \end{pmatrix} e^{i(\pm k_x^- x + k_y^- y)}, \tag{4.17}$$

where $\Psi_{h,\sigma}^+$ are left-going waves, while $\Psi_{h,\sigma}^-$ are right-going waves. The direction of the wave-function is determined by the group velocity like we did in section 2.2.3. As we will only consider energies below the gap, $E_{\boldsymbol{k}} < \Delta$, the wave vectors (2.17) will get imaginary parts and must decay in the superconductors. Consequently there will be no incoming wave-functions from the superconductor into the normal metal with such energies and we need only to consider the outgoing wave-functions in the superconducting regions. We let $k_y^+ \approx k_y^- \equiv k_y$ and the total wave functions

in the left (L) and right (R) region will thus be

$$\begin{aligned}\Psi_L(x-L/2,y) &= \Psi_L(x-L/2)e^{ik_y y}\\ \Psi_R(x+L/2,y) &= \Psi_R(x+L/2)e^{ik_y y}\end{aligned} \tag{4.18}$$

with $\Psi_{L/R}(x \mp L/2)$ given as

$$\begin{aligned}\Psi_L(x-L/2) &= a_1\begin{pmatrix} e^{i(\eta+\varphi_L)}\\ 0\\ 0\\ 1\end{pmatrix}e^{-ik_x^+ x} + a_2\begin{pmatrix} 0\\ e^{i(\eta+\varphi_L)}\\ -1\\ 0\end{pmatrix}e^{-ik_x^+ x} + a_3\begin{pmatrix} 1\\ 0\\ 0\\ e^{i(\eta-\varphi_L)}\end{pmatrix}e^{ik_x^- x} + a_4\begin{pmatrix} 0\\ -1\\ e^{i(\eta-\varphi_L)}\\ 0\end{pmatrix}e^{ik_x^- x}\\ \Psi_R(x+L/2) &= b_1\begin{pmatrix} e^{i(\eta+\varphi_R)}\\ 0\\ 0\\ 1\end{pmatrix}e^{ik_x^+ x} + b_2\begin{pmatrix} 0\\ e^{i(\eta+\varphi_R)}\\ -1\\ 0\end{pmatrix}e^{ik_x^+ x} + b_3\begin{pmatrix} 1\\ 0\\ 0\\ e^{i(\eta-\varphi_R)}\end{pmatrix}e^{-ik_x^- x} + b_4\begin{pmatrix} 0\\ -1\\ e^{i(\eta-\varphi_R)}\\ 0\end{pmatrix}e^{-ik_x^- x}.\end{aligned} \tag{4.19}$$

We have allowed for different phases φ_L and φ_R in each region and absorbed a phase factor $\exp(\pm ik_x L/2)$ in the coefficients in order to simplify the boundary equations.

4.2.3 Wave functions in the normal region

In the normal region the gap parameter, Δ, is zero, and so $u_0 = 1$ and $v_0 = 0$. The eigenvalues are $E_{\boldsymbol{k}} = \pm\varepsilon^{\pm}$ and the corresponding eigenvectors are

$$\Psi_{e,\uparrow}(\boldsymbol{r}) = \begin{pmatrix}1\\0\\0\\0\end{pmatrix}e^{i\boldsymbol{k}^+\cdot\boldsymbol{r}},\quad \Psi_{e,\downarrow}(\boldsymbol{r}) = \begin{pmatrix}0\\1\\0\\0\end{pmatrix}e^{i\boldsymbol{k}^+\cdot\boldsymbol{r}},\quad \Psi_{h,\uparrow}(\boldsymbol{r}) = \begin{pmatrix}0\\0\\1\\0\end{pmatrix}e^{i\boldsymbol{k}^-\cdot\boldsymbol{r}},\quad \Psi_{h,\downarrow}(\boldsymbol{r}) = \begin{pmatrix}0\\0\\0\\1\end{pmatrix}e^{i\boldsymbol{k}^-\cdot\boldsymbol{r}}. \tag{4.20}$$

We must here allow both right- and leftgoing waves and the total wave function in the normal region becomes

$$\Psi_N(x-L/2,y) = \Psi_N(x-L/2)e^{ik_y y} \tag{4.21}$$

with

$$\begin{aligned}\Psi_N(x-L/2) = c_1\begin{pmatrix}1\\0\\0\\0\end{pmatrix}e^{ik^+x} + c_2\begin{pmatrix}1\\0\\0\\0\end{pmatrix}e^{-ik^+x} + c_3\begin{pmatrix}0\\1\\0\\0\end{pmatrix}e^{ik^+x} + c_4\begin{pmatrix}0\\1\\0\\0\end{pmatrix}e^{-ik^+x}\\ + c_5\begin{pmatrix}0\\0\\1\\0\end{pmatrix}e^{ik^-x} + c_6\begin{pmatrix}0\\0\\1\\0\end{pmatrix}e^{-ik^-x} + c_7\begin{pmatrix}0\\0\\0\\1\end{pmatrix}e^{ik^-x} + c_8\begin{pmatrix}0\\0\\0\\1\end{pmatrix}e^{-ik^-x}.\end{aligned} \tag{4.22}$$

4.2.4 ABS energy

As we now have identified the wave functions in each region we are ready to use them in the boundary condition found in section 4.2.1:

$$\begin{aligned}&\Psi_L(-L/2) - \Psi_N(-L/2) = 0\\ &\Psi_R(L/2) - \Psi_N(L/2) = 0\\ &\frac{\partial\Psi_N(x)}{\partial x}\Big|_{x=-L/2} - \frac{\partial\Psi_L(x)}{\partial x}\Big|_{x=-L/2} - Z_L k_x \Psi_L(-L/2) = 0\\ &\frac{\partial\Psi_R(x)}{\partial x}\Big|_{x=L/2} - \frac{\partial\Psi_N(x)}{\partial x}\Big|_{x=L/2} - Z_R k_x \Psi_R(L/2) = 0.\end{aligned} \tag{4.23}$$

We insert the equations in a homogeneous matrix equation of the form

$$\mathrm{M}\big(a_1\cdots a_4\ b_1\cdots b_4\ c_1\cdots c_8\big)^T = 0 \tag{4.24}$$

where M is a 16×16-matrix. In the calculations all states are taken to be at the Fermi surface, $k_x^+ \approx k_x^- \equiv k_x$, and the barrier strengths

$$Z_L = \frac{2mV_L}{\hbar^2 k_x^2} \quad \text{and} \quad Z_R = \frac{2mV_R}{\hbar^2 k_x^2} \tag{4.25}$$

are introduced. The determinant of M can be found using an algebraic tool, giving

$$\det(\mathrm{M}) = \left(8e^{i\eta}\right)^4\left[\sin^2\frac{\Delta\varphi}{2} - (1+\zeta)\sin^2\eta\right]^2 \tag{4.26}$$

where we have introduced ζ, which measures the effect of the barriers and is given as

$$\zeta = Z^2 + z^2\sin(k_F L)\left[Z\cos(k_F L) + \left(\frac{z^2}{4} - 1\right)\sin(k_F L)\right] \tag{4.27}$$

with Z and z defined as

$$Z = \frac{Z_L + Z_R}{2} \quad \text{and} \quad z = \sqrt{Z_L Z_R}. \tag{4.28}$$

In order for the equations to have non-trivial solution the determinant (4.26) be zero and by inserting for $\eta = \arccos(E_{\boldsymbol{k}}/\Delta)$ and solving for $E_{\boldsymbol{k}}$ we find the energy levels:

$$E_{\boldsymbol{k}} = \Delta\cos\eta = \Delta\sqrt{\frac{\cos^2\frac{\Delta\varphi}{2} + \zeta}{\zeta + 1}}. \tag{4.29}$$

In the limit with no barrier, i.e. $\zeta = 0$, we see that equation (4.29) yields (4.7).

4.3 ABS energies with applied field

We will now apply a magnetic field, $\boldsymbol{B}(x, y)$, to the junction, and let the barriers be transparent. This imply modifying the Hamiltonian in the normal region to

$$h_N(\boldsymbol{r}) = \frac{1}{2m_N}\left(\frac{\hbar}{i}\nabla - q\boldsymbol{A}(\boldsymbol{r}, t)\right)^2 + qv(\boldsymbol{r}, t) - \mu_N \tag{4.30}$$

with $\boldsymbol{A}$ as the vector potential and v as the scalar potential.

Our strategy now is the same as in section 4.1. We want to express the problem in the phase of the wave function and use the quantization condition to find the energy.

4.3.1 Gauge transformation

$\boldsymbol{A}$ and v must be gauge invariant and we may do the following transformation

$$\begin{aligned} \boldsymbol{A}' &= \boldsymbol{A} + \nabla\chi \\ v' &= v - \frac{\partial\chi}{\partial t} \end{aligned} \tag{4.31}$$

where χ is any function of position and time. Such a transformation implies a transformation in the wavefunction Ψ as well. Considering the time-dependent Schrödinger equation yields

$$\begin{aligned} i\hbar\frac{\partial\Psi}{\partial t} &= \left[\frac{1}{2m}\left(\frac{\hbar}{i}\nabla - q\boldsymbol{A}\right)^2 + qv - \mu_N\right]\Psi \\ &= \left[\frac{1}{2m}\left(\frac{\hbar}{i}\nabla - q\boldsymbol{A}' + q\nabla\chi\right)^2 + qv' + q\frac{\partial\chi}{\partial t} - \mu_N\right]\Psi, \end{aligned} \tag{4.32}$$

which by rearranging and using that

$$e^{iq\chi/\hbar}\left(\frac{\hbar}{i}\nabla+q\nabla\chi\right)\Psi=\frac{\hbar}{i}\nabla\left(e^{iq\chi/\hbar}\Psi\right). \tag{4.33}$$

gives

$$\begin{aligned} i\hbar\frac{\partial}{\partial t}\left(\Psi e^{iq\chi/\hbar}\right) &= e^{iq\chi/\hbar}\left[\frac{1}{2m}\left(\frac{\hbar}{i}\nabla-q\boldsymbol{A}'+q\nabla\chi\right)^2+qv'\right]\Psi \\ &= \left[\frac{1}{2m}\left(\frac{\hbar}{i}\nabla-q\boldsymbol{A}'\right)^2+qv'\right]\left(\Psi e^{iq\chi/\hbar}\right). \end{aligned} \tag{4.34}$$

The Schrödinger equation in the transformed system is now on the same form as the original system:

$$i\hbar\frac{\partial\Psi'}{\partial t}=\left[\frac{1}{2m}\left(\frac{\hbar}{i}\nabla-q\boldsymbol{A}'\right)^2+qv'\right]\Psi' \tag{4.35}$$

with the transformed wave function $\Psi'=e^{iqf/\hbar}\Psi$. Thus a gauge transformation $\boldsymbol{A}\rightarrow\boldsymbol{A}+\nabla\chi$ imply a transformation $\phi\rightarrow\phi+q\chi/\hbar$ in the phase. The gauge invariant phase will be on the form

$$\phi_{\mathrm{GI}}=\phi-\frac{q}{\hbar}\int\boldsymbol{A}\cdot d\boldsymbol{r}, \tag{4.36}$$

as a transformation $\phi\rightarrow\phi+q\chi/\hbar$ and $\boldsymbol{A}\rightarrow\boldsymbol{A}+\nabla\chi$ give

$$\begin{aligned} \phi_{\mathrm{GI}}\rightarrow\phi+\frac{q}{\hbar}\chi-\frac{q}{\hbar}\int\left(\boldsymbol{A}+\nabla\chi\right)\cdot d\boldsymbol{r} &= \phi-\frac{q}{\hbar}\int\boldsymbol{A}\cdot d\boldsymbol{r}+\frac{q}{\hbar}\chi-\frac{q}{\hbar}\chi \\ &= \phi-\frac{q}{\hbar}\int\boldsymbol{A}\cdot d\boldsymbol{r}. \end{aligned} \tag{4.37}$$

We have in the previous sections taken $\boldsymbol{A}$ to be zero so that $\phi_{\mathrm{GI}}=\phi$. However, now that the magnetic field is non-zero we must include the vector potential in the phase. It is understood that the new term in the phase will be included in the energies and the supercurrent in the same way as the superconducting phase, such that the magnetic field is expected to be a driving force of the Josephson current in a similar manner as the superconducting phase.

4.3.2 Bohr-Sommerfeld quantization condition

Using the same method as in equation (4.5), but with the gauge invariant phase we get the quantization condition

$$\begin{aligned} 2\pi n=\oint d\phi &= \int_L^R\pm\boldsymbol{k}^{\pm}\cdot d\boldsymbol{l}\pm\frac{e}{\hbar}\int_L^R\boldsymbol{A}\cdot d\boldsymbol{l}+\phi^R_{(eh)(he)}+\int_R^L\pm\boldsymbol{k}^{\mp}\cdot d\boldsymbol{l}\mp\frac{e}{\hbar}\int_R^L\boldsymbol{A}\cdot d\boldsymbol{l}+\phi^L_{(he)(eh)} \\ &= L(k_x^+-k_x^-)+L\tan\theta(k_y^+-k_y^-)-2\eta\pm\left(\Delta\varphi+\frac{2e}{\hbar}\int_L^R\boldsymbol{A}\cdot d\boldsymbol{l}\right), \end{aligned} \tag{4.38}$$

where $\pm e$ is the charge of an electron (hole). Again, we let $k_x^+ \approx k_x^-$ and $k_y^+ \approx k_y^-$ and are left with

$$2\pi n = -2\eta \pm \left(\Delta\varphi - \gamma\right), \tag{4.39}$$

where

$$\gamma = -\frac{2e}{\hbar}\int_L^R \boldsymbol{A}\cdot d\boldsymbol{l} \tag{4.40}$$

is the Aharonov-Bohm phase shift [45]. We have assumed the curvature of the electrons, due to the Lorentz force, to be much larger than the length of the junction, so that we can neglect the effect the field has on the trajectory of the electrons/holes, and thus use the trajectories illustrated in figure 3.1.

4.3.3 ABS energy

The energy levels are found by inserting for η in equation (4.39) and solving for $E_{\boldsymbol{k}}$:

$$E_{\boldsymbol{k}} = \Delta\cos\eta = \Delta\cos\left(\frac{\Delta\varphi}{2} - \frac{\gamma}{2}\right). \tag{4.41}$$

Hence, the magnetic field add a phase shift to the superconducting phase difference and we notice that when the field is zero, i.e. $\gamma = 0$, the expression from equation (4.7) is reobtained.

Chapter 5

Andreev bound state current in an SNS-junction

We will in this chapter find the current of the system described in chapter 3 and 4 [1]. In chapter 2.4 we saw how the Josephson current can be expressed in terms of the free energy and the superconducting phase difference (2.34) and in chapter 2.5 the free energy was expressed in terms of the energy levels, $E_{\boldsymbol{k}}$ (2.39). Combining equation (2.34) and (2.39) we can thus express the Josephson current in terms of the ABS energies and the phase difference:

$$\begin{aligned} I_x(\Delta\varphi) &= \sum_{k_y} \delta I(\boldsymbol{r},\boldsymbol{k}) \to \int dy \int \frac{dk_y}{2\pi} \delta I(\boldsymbol{r},\boldsymbol{k}), \\ I_y(\Delta\varphi) &= \sum_{k_x} \delta I(\boldsymbol{r},\boldsymbol{k}) \to \int dx \int \frac{dk_x}{2\pi} \delta I(\boldsymbol{r},\boldsymbol{k}), \end{aligned} \tag{5.1}$$

where we have defined

$$\delta I(\boldsymbol{r},\boldsymbol{k}) \equiv -\frac{2e}{\hbar} \tanh\left(\frac{E_{\boldsymbol{k}}}{2k_B T}\right) \frac{\partial E_{\boldsymbol{k}}}{\partial(\Delta\varphi)}. \tag{5.2}$$

Since we have assumed $W \gg L$, I_y should be zero due to current conservation. The current density will be given as

$$\begin{aligned} j_x(x_0,y_0) &= \int \frac{dk_y}{2\pi} \delta I(\boldsymbol{r},\boldsymbol{k}) = \frac{k_F}{2\pi} \int_{-\pi/2}^{\pi/2} d\theta_k \cos\theta_k \delta I(\boldsymbol{r},\boldsymbol{k}), \\ j_y(x_0,y_0) &= \int \frac{dk_x}{2\pi} \delta I(\boldsymbol{r},\boldsymbol{k}) = \frac{k_F}{2\pi} \int_{-\pi/2}^{\pi/2} d\theta_k \sin\theta_k \delta I(\boldsymbol{r},\boldsymbol{k}), \end{aligned} \tag{5.3}$$

in the x- and y-direction, respectively, where we have let

$$\begin{pmatrix} dk_x \\ dk_y \end{pmatrix} \to k_F \begin{pmatrix} \sin\theta_k \\ \cos\theta_k \end{pmatrix} d\theta_k \tag{5.4}$$

[1] The calculations done in this chapter is inspired by the approach used by Ostroukh et. al (2016) [28].

as we consider the circular Fermi surface, as stated in chapter 3.

In chapter 4 the ABS energy levels were found for the three different situations and we will use these energies in equation (5.3) to find the current density and in equation (5.1) to find the total and critical current for each of the three situations. For the analytical progress we will consider the high temperature regime, ($k_B T \gtrsim \Delta$), in which the analytical calculations are simpler.

5.1 ABS current without barriers or applied field

In the case with no barriers or magnetic field we use the energy found in equation (4.7) in equation (5.2) to obtain

$$\delta I = \frac{e\Delta}{\hbar} \sin\left(\frac{\Delta\varphi}{2}\right) \tanh\left(\frac{\Delta\cos(\Delta\varphi/2)}{2k_B T}\right), \tag{5.5}$$

which we notice is independent of the trajectory of the particle. From equation (5.3) one finds the current density to be zero in the y-direction, $j_y(x,y) = 0$, and uniform in the x-direction, $j_x(x,y) = I_x/W$, where W is the junction width (indicated in figure 3.1) and I_x is the total current:

$$I_x = k_F W \frac{e\Delta}{\pi\hbar} \sin\left(\frac{\Delta\varphi}{2}\right) \tanh\left(\frac{\Delta\cos(\Delta\varphi/2)}{2k_B T}\right). \tag{5.6}$$

In the high temperature regime ($k_B T \gtrsim \Delta$) this can be approximated to

$$I_x = k_F W \frac{e\Delta}{\pi\hbar} \sin\left(\frac{\Delta\varphi}{2}\right) \frac{\Delta\cos(\Delta\varphi/2)}{2k_B T} = I_{c,0} \sin\Delta\varphi \tag{5.7}$$

with the high temperature critical current

$$I_{c,0} = \frac{k_F W e\Delta^2}{4\pi\hbar k_B T}. \tag{5.8}$$

These results are well known [44] and will be used for comparison in the preceding sections.

5.2 ABS current with barriers

The ABS energy levels in the case of barriers was found in equation (4.29). Inserting this in equation (5.2) yields

$$\delta I = \frac{e\Delta}{2\hbar} \frac{\sin(\Delta\varphi)}{\sqrt{(\cos^2(\Delta\varphi/2)+\zeta)(\zeta+1)}} \tanh\left(\frac{\Delta}{2k_B T}\sqrt{\frac{\cos^2(\Delta\varphi/2)+\zeta}{\zeta+1}}\right). \tag{5.9}$$

Also here δI is independent of the trajectory such that the current density is uniform. The total current is

$$I_x = k_F W \frac{e\Delta}{2\pi\hbar} \frac{\sin(\Delta\varphi)}{\sqrt{(\cos^2(\Delta\varphi/2)+\zeta)(\zeta+1)}} \tanh\left(\frac{\Delta}{2k_BT}\sqrt{\frac{\cos^2(\Delta\varphi/2)+\zeta}{\zeta+1}}\right), \tag{5.10}$$

so that the high temperature critical current is

$$I_{c,\zeta} = \frac{k_F W e\Delta^2}{4\pi\hbar k_B T}\frac{1}{\zeta+1} = \frac{I_{c,0}}{\zeta+1}, \tag{5.11}$$

with $I_{c,0}$ as the critical current without barriers (5.8). Figure 5.1 shows how the total current varies with the phase difference, $\Delta\varphi$, in the high temperature regime ($k_BT = \Delta$) for different barrier strengths, ζ.

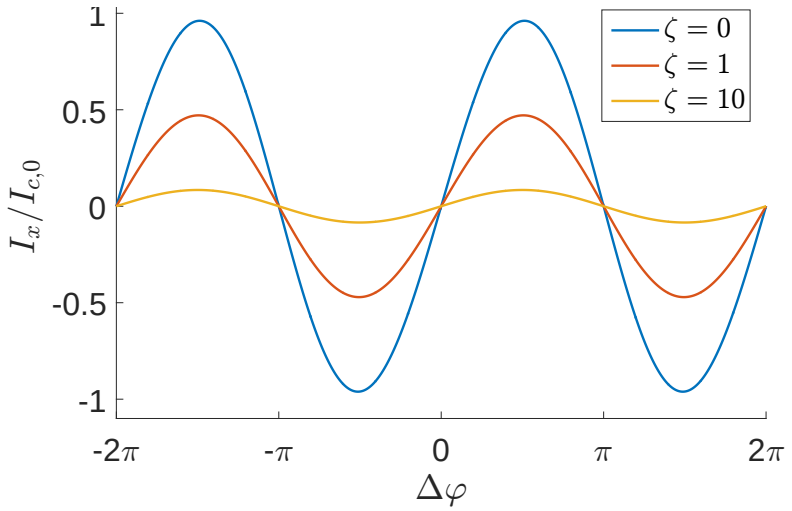

Figure 5.1: Plot of the total supercurrent I_x versus the superconducting phase difference $\Delta\varphi$ through the normal region of the Josephson junction at temperature $k_BT = \Delta$. The current is calculated from equation (5.10) for different barrier strengths, ζ, at the superconducting interface.

5.3 ABS current with applied field

With no barriers, but magnetic field we find the current from the ABS energy in equation (4.41):

$$\delta I_k(\Delta\varphi) = \frac{e\Delta}{\hbar}\sin\left(\frac{\Delta\varphi}{2}-\frac{\gamma_k}{2}\right)\tanh\left(\frac{\Delta\cos\left(\frac{\Delta\varphi}{2}-\frac{\gamma_k}{2}\right)}{2k_BT}\right) \tag{5.12}$$

which in the high temperature regime ($k_B T \gtrsim \Delta$), can be approximated to

$$\delta I_k(\Delta\varphi) \approx \frac{e\Delta^2}{4\hbar k_B T} \sin\left(\Delta\varphi - \gamma_k\right). \tag{5.13}$$

The Aharonov-Bohm phase shift, γ_k, will depend on the modulation and strength of the magnetic field, as well as the trajectory of the particle. We will here consider three different modulations of the magnetic field. That is a uniform magnetic field (section 5.3.1), sinusoidal field varying along the junction (section 5.3.2) and sinusoidal field varying along the interfaces (section 5.3.3).

The magnetic field will be expelled in the superconducting region, due to the Meissner effect. We assume the penetration depth to be short even in the high-field regime, i.e. when $l_m \lesssim L$ with with $l_m = \sqrt{\hbar/eB}$ as the magnetic length. The Lorentz effect will change the trajectories in the magnetic field into arcs of cyclotron radius $l_{\text{cycl}} = \hbar k_F / eB = k_F l_m^2$. However, we assume that $k_F L$ is sufficiently large such that $l_{\text{cycl}}/L = k_F L (l_m/L)^2 \gg 1$ for the fields considered and we can neglect the curvature of the trajectories.

5.3.1 Uniform magnetic field

We will first consider a uniform magnetic field of strength B in the normal region:

$$\boldsymbol{B} = B\left[\Theta(x + L/2) - \Theta(x - L/2)\right]\hat{z}, \tag{5.14}$$

and choose the gauge of the $\boldsymbol{A}$-field as

$$\boldsymbol{A} = -By\left[\Theta(x + L/2) - \Theta(x - L/2)\right]\hat{x}. \tag{5.15}$$

The Aharonov-Bohm phase shift, $\gamma(x_0, y_0, \theta_k)$, is calculated from equation (4.40) by integration along a path through the point (x_0, y_0) at an angle θ_k with the x-axis, as shown in figure 3.1. The trajectory will be given by the line

$$y(x) = y_0 - x_0 \tan\theta_k + x \tan\theta_k, \tag{5.16}$$

and using this in equation (4.40) we find the phase shift:

$$\begin{aligned} \gamma &= -\frac{2e}{\hbar}\int_L^R \boldsymbol{A}\cdot d\boldsymbol{l} = B\frac{2e}{\hbar}\int_{-L/2}^{L/2} y(x)\,dx \\ &= \frac{2L}{l_m^2}\left(y_0 - x_0\tan\theta_k\right). \end{aligned} \tag{5.17}$$

This expression is used in equation (5.12) and (5.3) in order to find the current density. The result from numerical computation is shown in figure 5.2 for three different magnetic lengths revealing

the appearance of a chain of current vortex-antivortex pairs. We emphasize here that we are discussing supercurrent vortices which are distinct from Abrikosov vortices, the latter having normal cores and a phase-winding of 2π in the superconducting order parameter. The distance, d_{vortex}, between two vortices positioned at y_0 and $y_0 + d_{\text{vortex}}$, respectively, will satisfy the relation

$$\gamma(y_0 + d_{\text{vortex}}) = \gamma(y_0) + 2\pi \tag{5.18}$$

as this gives equal current in the vortices according to equation (5.13). By inserting for γ we find the vortex distance

$$d_{\text{vortex}} = \pi \frac{l_m^2}{L}, \tag{5.19}$$

and it is clear that the distance between the vortices increases with the magnetic length, as observed in figure 5.2. In the figure we have chosen the phase difference to be $\Delta\varphi = \pi/2$. A change $\delta\varphi$ in $\Delta\varphi$ would give a shift along the y-axis:

$$\delta I_k(y_0, \Delta\varphi + \delta\varphi) = \delta I_k\left(y_0 - \frac{l_m^2}{2L}, \delta\varphi\right), \tag{5.20}$$

as we from equation (5.12) have

$$\delta I_k(y_0, \Delta\varphi + \delta\varphi) = \frac{e\Delta}{\hbar} \sin\left(\frac{\Delta\varphi}{2} - \frac{\gamma_k - \delta\varphi}{2}\right) \tanh\left(\frac{\Delta \cos\left(\frac{\Delta\varphi}{2} - \frac{\gamma_k - \delta\varphi}{2}\right)}{2k_B T}\right) \tag{5.21}$$

and

$$\gamma_k(y_0) - \delta\varphi = \frac{2L}{l_m^2}\left(y_0 - \frac{l_m^2}{2L}\delta\varphi - x_0 \tan\theta_k\right) = \gamma_k\left(y_0 - \frac{l_m^2}{2L}\delta\varphi\right). \tag{5.22}$$

However, the linear vortex pattern remains.

In order to find the total current we combine equation (5.1), (5.3) and (5.12):

$$I_x = \frac{k_F}{2\pi}\frac{e\Delta}{\hbar}\int_{-W/2}^{W/2} dy_0 \int_{-\pi/2}^{\pi/2} d\theta_k \cos\theta_k \sin\left(\frac{\Delta\varphi}{2} - \frac{\gamma}{2}\right) \tanh\left(\frac{\Delta}{2k_B T}\cos\left(\frac{\Delta\varphi}{2} - \frac{\gamma}{2}\right)\right), \tag{5.23}$$

which in the high temperature regime ($k_B T \gtrsim \Delta$) is simplified to

$$I_x = \frac{I_{c,0}}{2W}\int_{-W/2}^{W/2} dy_0 \int_{\pi/2}^{\pi/2} d\theta_k \cos\theta_k \sin(\Delta\varphi - \gamma). \tag{5.24}$$

From equation (5.17) we notice that $\gamma(x_0, y_0, \theta_k) = -\gamma(x_0, -y_0, -\theta_k)$ which allows us to write

$$I_x = \frac{I_{c,0}}{W}\sin(\Delta\varphi)\int_{-W/2}^{W/2} dy_0 \int_0^{\pi/2} d\theta_k \cos\theta_k \cos\gamma. \tag{5.25}$$

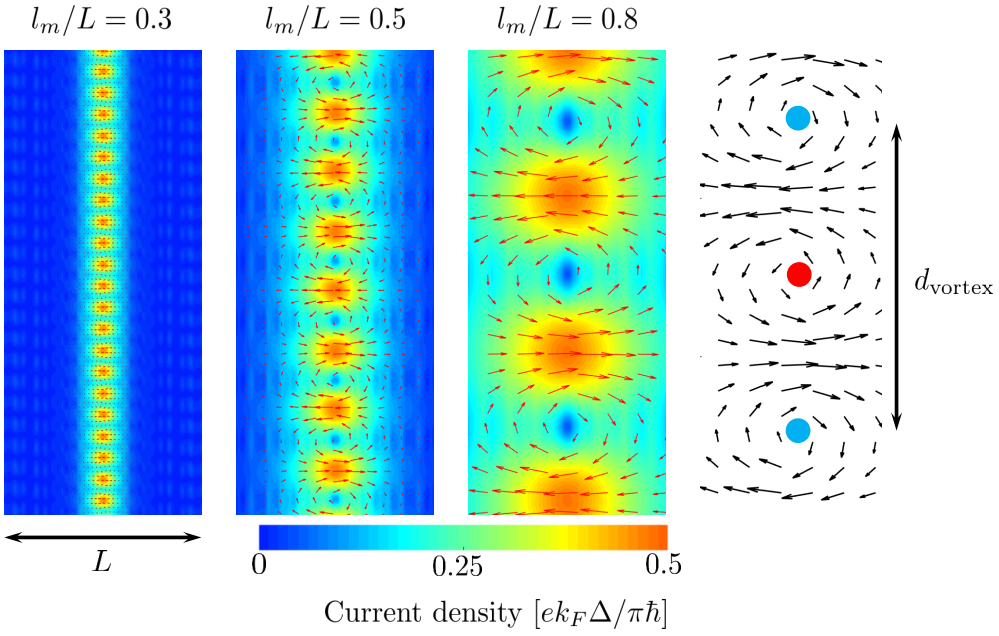

Figure 5.2: The three scale plots show the supercurrent density in a wide Josephson junction, far from the lateral boundaries for three values of the magnetic field ($l_m/L = 0.3,\ 0.5$ and 0.8). The plots are calculated numerically from equation (5.3), (5.12) and (5.17) at $k_B T = \Delta$. In the plot to the right the current density of magnetic field $l_m/L = 0.8$ is also illustrated with velocity vectors indicating the vortices and anti-vortices, along with the vortex distance $d_{\text{vortex}} = \pi l_m^2/L$.

The integral over y_0 gives

$$\int_{-W/2}^{W/2} dy_0 \cos\gamma = \frac{l_m^2}{L}\sin\left(\frac{LW}{l_m^2}\right)\cos\left(\frac{2L}{l_m^2}x_0\tan\theta_k\right) \approx \frac{l_m^2}{L}\sin\left(\frac{LW}{l_m^2}\right), \tag{5.26}$$

where the last equality is taken in the low field regime ($l_m \gg L$) in order to simplify the analytical expression. The total current is thus

$$I_x = I_{c,0}\frac{\sin\left(\frac{e}{\hbar}\Phi\right)}{\frac{e}{\hbar}\Phi}\sin\Delta\varphi \tag{5.27}$$

with $\Phi = BLW$ as the magnetic flux and we find the critical current at $\Delta\varphi = \pi/2$:

$$I_{c,\text{const}} = I_{c,0}\left|\frac{\sin\left(\frac{e}{\hbar}\Phi\right)}{\frac{e}{\hbar}\Phi}\right| \tag{5.28}$$

which is the well known Fraunhofer oscillations. By comparing the period $\Phi_0 = \pi\hbar/e$ with the vortex distance d_{vortex} from equation (5.19) we find the relation

$$d_{\text{vortex}} = W\frac{\Phi_0}{\Phi}. \tag{5.29}$$

This result relate the vortex pattern distance, d_{vortex}, to the period, Φ_0, of the Fraunhofer oscillations and we realize that the oscillations are a direct consequence of the vortex pattern. The critical current resulting from numerical calculations is shown in figure 5.3.

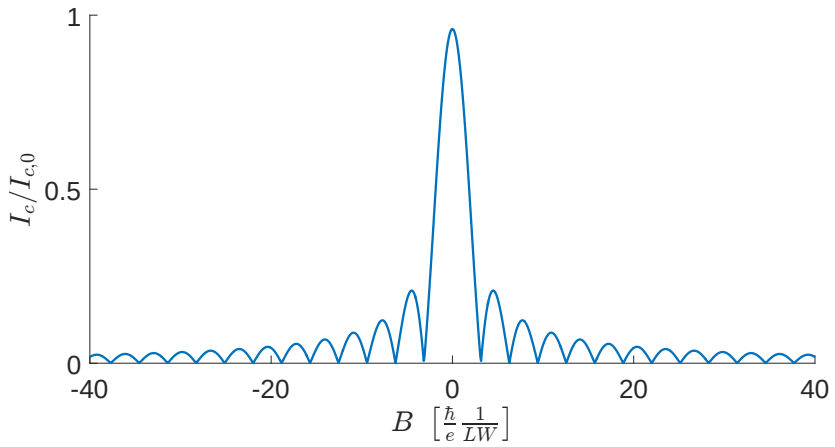

Figure 5.3: Plot of the critical current I_c through the normal region versus the magnetic field strength B in a uniform field. The current is calculated numerically from equation (5.1), (5.12) and (5.17) at $\Delta\varphi = \pi/2$.

5.3.2 Sinusoidal field varying along the junction

All of the preceding results are already well known. In the following we will take the magnetic field to be non-uniform and see that this reveals new and interesting phenomena. We start by considering a sinusoidal magnetic field, of wavelength λ, along the junction (see figure 5.4):

$$\boldsymbol{B} = B\sin\left(\frac{2\pi}{\lambda}x+\chi\right)\left[\Theta(x+L/2)-\Theta(x-L/2)\right]\hat{z} \tag{5.30}$$

with the gauge

$$\boldsymbol{A} = -By\sin\left(\frac{2\pi}{\lambda}x+\chi\right)\left[\Theta(x+L/2)-\Theta(x-L/2)\right]\hat{x}. \tag{5.31}$$

Like we did for the uniform field we use equation (4.40) and integrate along the trajectory in (5.16) to find the Aharonov-Bohm phase shift:

$$\begin{aligned}\gamma &= \frac{2}{l_m^2}\int_{-L/2}^{L/2} y(x)\sin\left(\frac{2\pi}{\lambda}x+\chi\right)dx \\ &= \frac{2\lambda}{\pi l_m^2}\left(\left[y_0 - x_0\tan\theta_k\right]\sin\left(\frac{\pi L}{\lambda}\right)\sin\chi + \frac{L}{2}\tan\theta_k\left[\frac{\lambda}{\pi L}\sin\left(\frac{\pi L}{\lambda}\right)-\cos\left(\frac{\pi L}{\lambda}\right)\right]\cos\chi\right).\end{aligned} \tag{5.32}$$

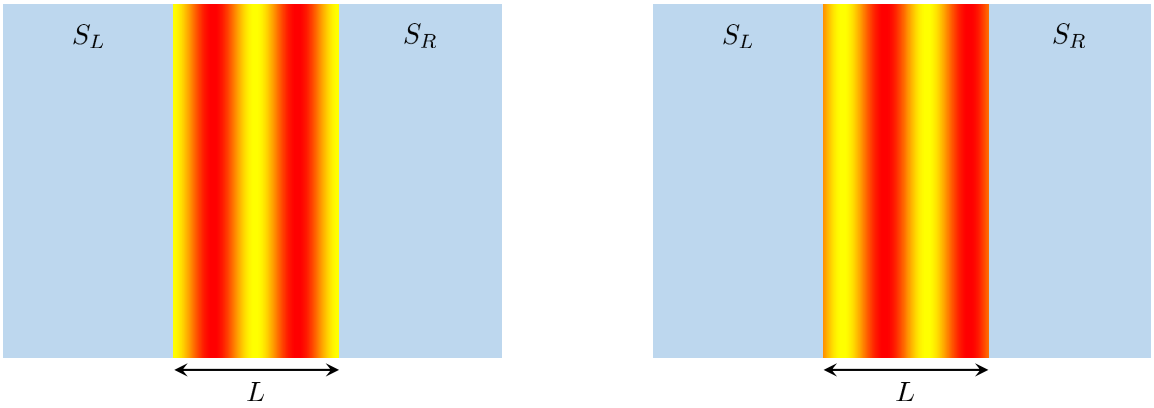

Figure 5.4: Scale plot of the external magnetic field varying periodically in the normal region along the junction. The scale plots are found from equation (5.30) with wavelength $\lambda = 0.5L$ and phase $\chi = \pi/2$ in the symmetric field (a) and $\chi = 0$ in the anti-symmetric field (b).

This expression has two terms, of which the second is independent of the position (x_0, y_0) and both are dependent on the wavelength, λ, and phase, χ, of the magnetic field.

Symmetric field

We start by considering a symmetric field about the y-axis and set $\chi = \pi/2$ in (5.30). The second term in equation (5.32) will in this modulation vanish such that the phase shift is

$$\gamma = \frac{2\lambda}{\pi l_m^2}\left[y_0 - x_0 \tan\theta_k\right] \sin\left(\frac{\pi L}{\lambda}\right) = \gamma_{\text{uni}} \frac{\sin(\pi L/\lambda)}{\pi L/\lambda} \tag{5.33}$$

where γ_{uni} is the Aharonov-Bohm phase shift in the uniform magnetic field as given in equation (5.17). As this expression is proportional to the phase shift for uniform field we expect appearance of current vortices, but with a vortex distance dependent on the wavelength of the magnetic field:

$$d_{\text{vortex}} = \pi \frac{l_m^2}{L} \left| \frac{\pi L/\lambda}{\sin(\pi L/\lambda)} \right|. \tag{5.34}$$

Hence, the distance between the vortices can be controlled not only by changing the magnetic field strength, but also by changing the wavelength of the symmetric field. For wavelengths $\lambda = L/n$, with n as an non-zero integer, we notice that $d_{\text{vortex}} \to \infty$ and $\gamma \to 0$, and **we expect the vortices to vanish completely and the current to be unaffected by the magnetic field, regardless of the magnetic field strength**.

The current density is calculated numerically by using γ (5.33) in equation (5.12) and (5.3) and the result is shown in figure 5.5 for three different wavelengths, λ. As we predicted analytically, the

distance between the vortices is changed when the wavelength of the magnetic field is changed, and we notice that for some wavelengths, e.g. $\lambda = L/2$, the vortices vanish completely.

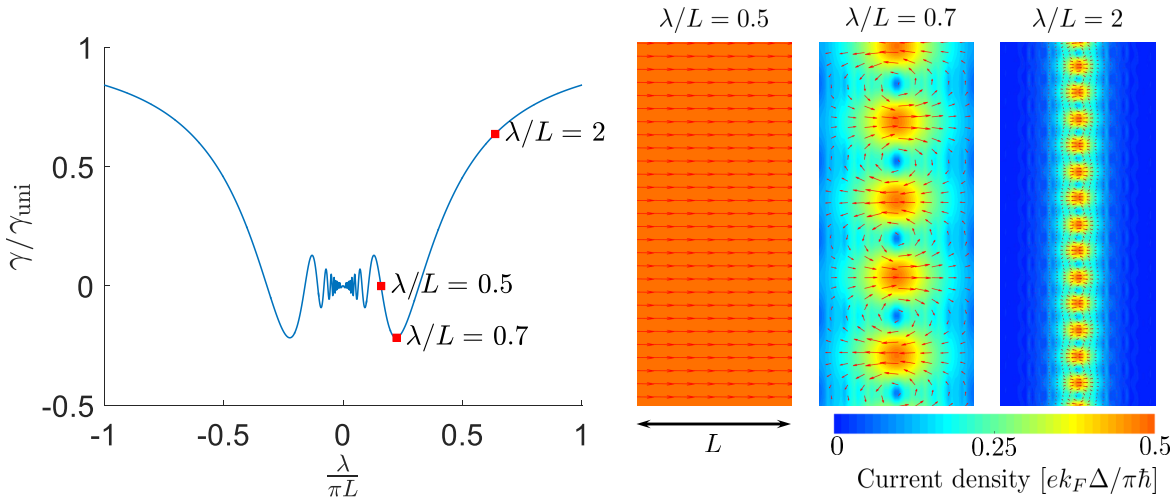

Figure 5.5: The left plot shows the phase shift γ, relative to the phase shift, γ_{uni}, in a uniform field, versus the wavelength λ of an applied sinusoidal magnetic field varying along the Josephson junction. The scale plots shows the current density in the junction for three different wavelengths λ, all for the same magnetic field strength $l_m/L = 0.3$. The wavelength of each scale plot is indicated in the γ-plot. When $\lambda = 0.5L$ the phase shift is $\gamma = 0$ and the current density is uniform. The γ-plot is calculated from equation (5.33) and the scale plots are calculated from equation (5.3), (5.12) and (5.33) at temperature $k_B T = \Delta$.

The total current is found in the same manner as in section 5.3.1, giving

$$I_x = I_{c,0} \sin\Delta\varphi \frac{\sin(\frac{e}{\hbar}\Phi)}{\frac{e}{\hbar}\Phi} \tag{5.35}$$

where Φ is the magnetic flux,

$$\Phi = \int \boldsymbol{B} \cdot d\boldsymbol{A} = \Phi_{\text{uni}} \frac{\sin(\pi L/\lambda)}{\pi L/\lambda}, \tag{5.36}$$

and $\Phi_{\text{uni}} = BWL$ is the magnetic flux in the uniform field. In terms of magnetic flux the critical current is identical to the total current in the uniform field. However, the flux, and consequently the total and critical current, is dependent on the wavelength, λ. The high temperature critical current will be given as

$$I_c = I_{c,0} \left| \frac{\sin\left(\frac{LW}{l_m^2} \frac{\sin(\pi L/\lambda)}{\pi L/\lambda}\right)}{\frac{LW}{l_m^2} \frac{\sin(\pi L/\lambda)}{\pi L/\lambda}} \right|. \tag{5.37}$$

We find the period of the Fraunhofer oscillations to be $d_{\text{vortex}}\Phi_{\text{uni}}/W$ with $\Phi_{\text{uni}} = BLW$, so that the Fraunhofer oscillations are related to the vortex pattern in the same manner as the uiform filed. In figure 5.6 the critical current obtained from numerical computation is shown for different wavelengths, λ, and varying magnetic field strength, B. We recognize the Fraunhofer pattern as we had for the uniform field, but the decay can be controlled by changing the wavelength, λ, and for some wavelengths, e.g. $\lambda = L/2$, the critical current maintains constant regardless of the field strength. We propose that this can be understood as an interference phenomenon where the phase-shift picked up by the electrons and holes comprising the ABS level are completely cancelled out due to the specific magnetic field profile. The fact that the supercurrent survives for arbitrarily large field strengths, B, as long as the spatial modulation wavelengths satisfy $\lambda = L/n$ is remarkable and is one of the key findings in this thesis.

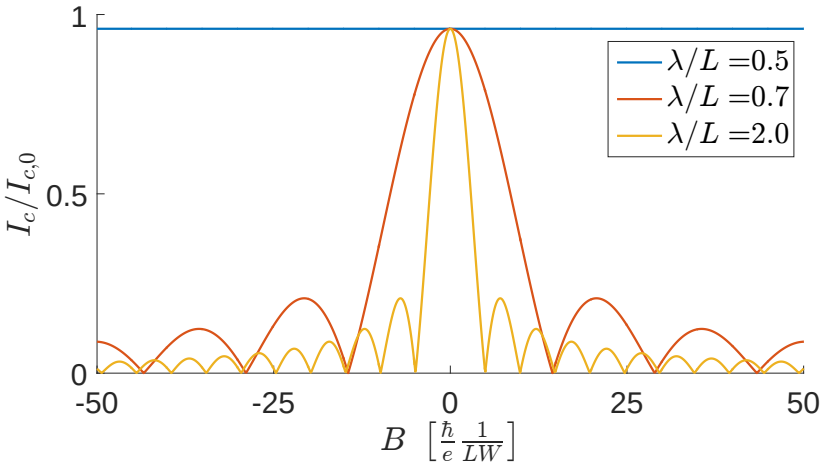

Figure 5.6: Plot of the critical current I_c versus the magnetic field strength B in a symmetric periodic field varying with three wavelengths, λ, along the junction in the normal region. The current is calculated numerically from equation (5.1), (5.12) and (5.33) at $\Delta\varphi = \pi/2$.

Anti-symmetric field

Taking χ to zero in (5.30) the magnetic field becomes anti-symmetric about the y-axis, and the first term in (5.32) vanishes:

$$\gamma = \frac{L^2}{l_m^2}\tan\theta_k\left[\left(\frac{\lambda}{\pi L}\right)^2\sin\left(\frac{\pi L}{\lambda}\right) - \frac{\lambda}{\pi L}\cos\left(\frac{\pi L}{\lambda}\right)\right]. \tag{5.38}$$

We notice how γ now is position-independent and expect a uniform current distribution without current vortices. The magnetic wavelength dependency of γ is shown in figure 5.7(a). For certain wavelengths, λ, γ will be zero regardless of the field strength or position and we expect the current

to be unaffected by the magnetic field. Using the expression for γ (5.38) in equation (5.12) and (5.3) the current density is found numerically and the result is shown in figure 5.7(b) for varying wavelengths, λ, of the external field.

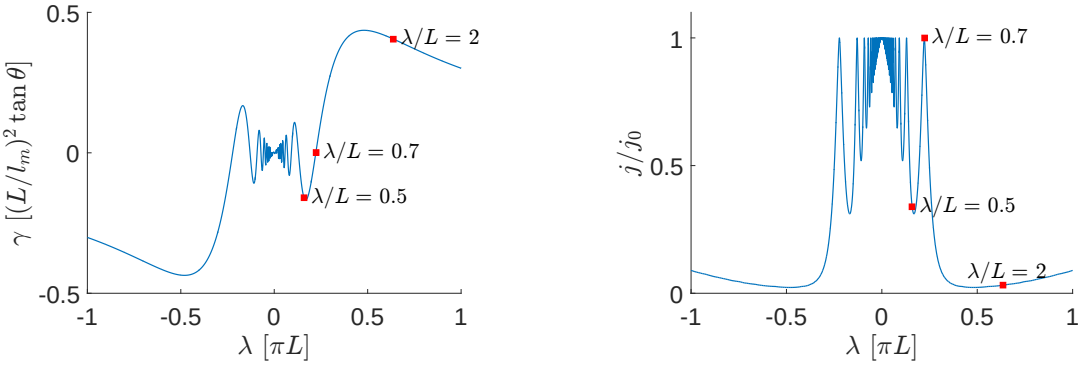

(a) (b)

Figure 5.7: Plot of the phase shift γ (a) and the uniform current density (b) versus the wavelength of an anti-symmetric applied magnetic field varying periodically along the junction. The γ-plot is calculated from equation (5.38) and the current density is calculated from equation (5.3), (5.12) and (5.38) at temperature $k_B T = \Delta$ and magnetic length $l_m/L = 0.3$. Three wavelengths ($\lambda/L = 0.5$, $\lambda/L = 0.7$ and $\lambda/L = 2$) are marked in each plot for comparison with figure 5.8.

We find the total current in the high temperature regime as we did for the uniform field in section 5.3.1. As γ (5.32) is independent of y_0, equation (5.24) yields

$$I = \frac{I_{c,0}}{2} \int_{-\pi/2}^{\pi/2} d\theta_k \cos\theta_k \sin(\Delta\varphi - \gamma). \tag{5.39}$$

Using that $\gamma(\theta_k) = -\gamma(-\theta_k)$ this can be rewritten to

$$I = I_{c,0} \sin\Delta\varphi \int_{0}^{\pi/2} d\theta_k \cos\theta_k \cos\gamma. \tag{5.40}$$

After inserting for γ and integrating over θ_k we obtain the total current,

$$I = I_{c,0} \sin\Delta\varphi \frac{L^2}{l_m^2} \left|f(\lambda)\right| K_1\left(\frac{L^2}{l_m^2}\left|f(\lambda)\right|\right), \tag{5.41}$$

where $K_1(z)$ is the modified Bessel function of second kind and we have defined

$$f(\lambda) \equiv \left(\frac{\lambda}{\pi L}\right)^2 \sin\left(\frac{\pi L}{\lambda}\right) - \frac{\lambda}{\pi L}\cos\left(\frac{\pi L}{\lambda}\right). \tag{5.42}$$

Hence, the high temperature critical current is

$$I_c = I_{c,0}\frac{L^2}{l_m^2}\left|f(\lambda)\right| K_1\left(\frac{L^2}{l_m^2}\left|f(\lambda)\right|\right). \tag{5.43}$$

The wavelengths λ that make $f(\lambda)$ go to zero, will give $I_c = I_{c,0}$, regardless of the magnetic field strength and the currnt will be unaffected by the magnetic field at these wavelengths. In figure 5.8 the critical current obtained from numerical computation is shown for different wavelengths, λ, and varying magnetic field strength, B. This numerical result is in correspondence with the analytical expression (5.43). We notice that in this modulation the Fraunhofer pattern vanishes and understand this as being a direct consequence of the absence of the current vortices. Like we found for the symmetric field there exists wavelengths, e.g. $\lambda \approx 0.7L$, which make the critical current I_c remain constant when the magnetic field strength increases.

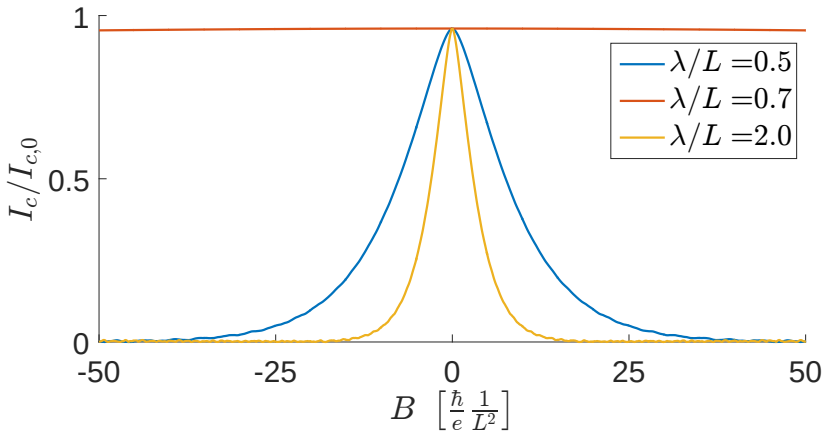

Figure 5.8: Plot of the critical current I_c versus the magnetic field strength B in a anti-symmetric periodic field varying with three wavelengths, λ, along the junction in the normal region. The current is calculated numerically from equation (5.1), (5.12) and (5.38) at $\Delta\varphi = \pi/2$.

5.3.3 Sinusoidal field varying along the interfaces

Instead of varying the field along the junction we will now consider a sinusoidal magnetic field varying along the interfaces (see figure 5.9):

$$\boldsymbol{B} = B\sin\left(\frac{2\pi}{\lambda}y + \chi\right)\left[\Theta(x + L/2) - \Theta(x - L/2)\right]\hat{z} \tag{5.44}$$

with the gauge

$$\boldsymbol{A} = B\frac{\lambda}{2\pi}\cos\left(\frac{2\pi}{\lambda}y + \chi\right)\left[\Theta(x + L/2) - \Theta(x - L/2)\right]\hat{x}. \tag{5.45}$$

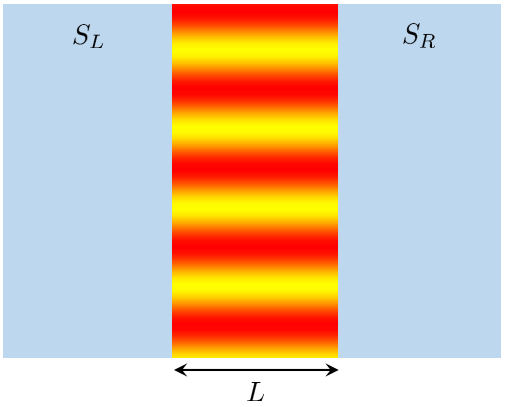

Figure 5.9: Scale plot of the external magnetic field varying periodically in the normal region along the interface. The scale plot is found from equation (5.44) with a wavelength $\lambda = 0.5L$.

In this field the Aharonov-Bohm phase shift is

$$\gamma = -\frac{\lambda L}{l_m^2 \pi} \frac{\sin\left(\frac{\pi L}{\lambda}\tan\theta_k\right)}{\frac{\pi L}{\lambda}\tan\theta_k} \cos\left(\frac{2\pi}{\lambda}\left[y_0 + \frac{\lambda}{2\pi}\chi - x_0\tan\theta_k\right]\right). \tag{5.46}$$

We notice that a change $\Delta\chi$ of the phase χ, is equivalent with a change $\Delta\chi\lambda/2\pi$ of the position y_0 along the interface. Hence, we expect the same current for any χ only with the pattern shifted along the interface. This is also reasonable as we consider a wide junction ($W \gg L$) and a phase shift of the field along W should not change the physics of the system.

Symmetric field

We will in the analytical process let $\chi = \pi/2$ in which the field is symmetric about the x-axis and then generalize the results for any χ. With $\chi = \pi/2$ the Aharonov-Bohm phase shift is

$$\gamma = \frac{\lambda L}{l_m^2 \pi} \frac{\sin\left(\frac{\pi L}{\lambda}\tan\theta_k\right)}{\frac{\pi L}{\lambda}\tan\theta_k} \sin\left(\frac{2\pi}{\lambda}\left[y_0 - x_0\tan\theta_k\right]\right). \tag{5.47}$$

In the limit with $\lambda \gg L$ and $\lambda \gg y_0$ the phase shift will approach the phase shift in the uniform field, $\gamma \to \gamma_{\text{uni}}$:

$$\gamma \to \frac{\lambda L}{l_m^2 \pi}\left(\frac{2\pi}{\lambda}\left[y_0 - x_0\tan\theta_k\right]\right) = \frac{2L}{l_m^2}\left(y_0 - x_0\tan\theta_k\right) \tag{5.48}$$

where we have used that $\sin(x) \approx x$ when $x \ll 1$. This is expected as a symmetric periodical function will be approximately uniform when the wavelength becomes very large. In the limit with $\lambda \ll L$ the sinc-function in the second factor of (5.47) will go to zero and the effect of the magnetic

field on the current will vanish.

In order to simplify the analytics we take θ_k to zero as this angle will contribute most to the current. In this approximation γ takes the form

$$\gamma = \frac{\lambda L}{l_m^2 \pi} \sin\left(\frac{2\pi}{\lambda} y_0\right). \tag{5.49}$$

We will soon see that the vortex distance in this field vary periodically along the y-axis, and write $d_{\text{vortex}} = d_{\text{vortex}}(y_0)$. The vortex distance can be found by the same approach used for the uniform field. Inserting for γ in the relation

$$\gamma\left(y_0 + d_{\text{vortex}}(y_0)\right) = \gamma(y_0) + 2\pi \tag{5.50}$$

and solving for d_{vortex} yields

$$d_{\text{vortex}}(y_0) = -y_0 + \frac{\lambda}{2\pi} \arcsin\left[\sin\left(\frac{2\pi}{\lambda} y_0\right) + 2\frac{l_m^2 \pi^2}{\lambda L}\right]. \tag{5.51}$$

In the limit of $\lambda \gg L$ and $\lambda \gg y_0$ the expression in (5.51) approaches the vortex distance in the uniform field:

$$\begin{aligned} d_{\text{vortex}} &\to -y_0 + \frac{\lambda}{2\pi} \arcsin\left(\frac{2\pi}{\lambda}\left[y_0 + \frac{l_m^2 \pi}{L}\right]\right) \\ &\to -y_0 + y_0 + \pi \frac{l_m^2}{L} \\ &= \pi \frac{l_m^2}{L} \end{aligned} \tag{5.52}$$

where we have used that $\sin x \approx x$ and $\arcsin x \approx x$ when $x \ll 1$. This is the vortex distance we found for the uniform field (5.19) and corresponds to the limit found in equation (5.48). We stated above that the vortex distance would vary periodically along the y-axis. This means that there is a distance, d_{chain}, which satisfy

$$d_{\text{vortex}}(y_0 + d_{\text{chain}}) = d_{\text{vortex}}(y_0) + m d_{\text{chain}}, \tag{5.53}$$

with m as an integer. From equation (5.51) we find that this is satisfied if we let $m = 1$ and $d_{\text{chain}} = \lambda$. Thus we expect the pattern to be *chains* of vortices separated by a y_0-dependent distance d_{vortex} and with each chain center separated by λ. Moreover, just like the vortices, the chains will also appear as chains and anti-chains, with the distance between neighboring chains and anti-chains $d_{\text{chain}}/2 = \lambda/2$. This can be seen from equation (5.47) in which we notice that $\gamma(y_0 + \lambda/2) = -\gamma(y_0)$. We will consider the center of a chain as the point where d_{vortex} is shortest, i.e. where the vortex

density is largest. From equation (5.51) we find d_{vortex} to be shortest at $y_0 = n\lambda$ and setting $n = 0$ we expect the first chain to be placed with its center at $y_0 = 0$.

Unlike we saw in the uniform field, the vortex pattern for the field considered here depend on the superconducting phase difference, $\Delta\varphi$. We check the dependency $\Delta\varphi$ has on the current density in the same manner as we did for the uniform field. That is we consider equation (5.12) in which we see that a phase difference $\delta\varphi$ in the superconducting phase corresponds to a phase shift $-\delta\varphi$ in γ. In the uniform field we found that such phase shift only gave a shift along the interface, $\gamma_{\text{uni}}(y_0) - \delta\varphi = \gamma_{\text{uni}}(y_0 - \delta\varphi l_m^2/2L)$, and the pattern remained. In the field considered in this section this relation does not apply and we expect the superconducting phase difference to affect the pattern. More specifically we can consider the relation between the chains and anti-chains. If we take $\Delta\varphi = 0$ we find from equation (5.13) that a shift $d_{\text{chain}}/2 = \lambda/2$, which would take us from a chain to an anti-chain (or the other way around), will give

$$\delta I(y_0 + \lambda/2) = \frac{I_{c,0}}{k_F W}\sin\big(\gamma(y_0 + \lambda/2)\big) = -\frac{I_{c,0}}{k_F W}\sin\big(\gamma\big) = -\delta I(y_0) \tag{5.54}$$

and the current in the anti-chain is in fact opposite of the current in the chain. However, if we take the superconducting phase difference to be $\Delta\varphi = \pi/2$, the current density is symmetrically dependent on γ:

$$\delta I(y_0 + \lambda/2) = \frac{I_{c,0}}{k_F W}\cos\big(\gamma(y_0 + \lambda/2)\big) = \frac{I_{c,0}}{k_F W}\cos\big(\gamma\big) = \delta I(y_0) \tag{5.55}$$

such that the current in the anti-chains and the chains are identical. The vortex pattern can in this case be thought of as a linear arrangement of only chains with centers separated by a distance $d_{\text{chain}} = \lambda/2$, in contrast to the chain- anti-chain arrangement we get if the the superconducting phase difference is zero.

The current density was found numerically from equation (5.12) and (5.3) and the result is shown in figure 5.10 for different wavelengths. We observe what was predicted, namely a repeated pattern of vortex- anti-vortex-chains along the interfaces. With $\Delta\varphi = 0$ we observe a chain- anti-chain pattern with each chain separated by $d_{\text{chain}} = \lambda$. With $\Delta\varphi = \pi/2$ there are no anti-chains as the current density is an even function of γ and each chain is separated by $\lambda/2$. Moreover, the current density approaches a uniform distribution as $\lambda \to 0$ with current as given in equation (5.7), as we predicted analytically. When $\lambda \gg L$ the uniform field pattern is reobtained, as predicted.
As the expression for γ is quite complicated we can not calculate the total current analytically, even in the high temperature regime. However, the critical current is found numerically and the result is shown in figure 5.11. For large wavelengths, λ, the critical current approaches the Fraunhofer pattern as we would expect from the pattern we found in the current density. The critical current

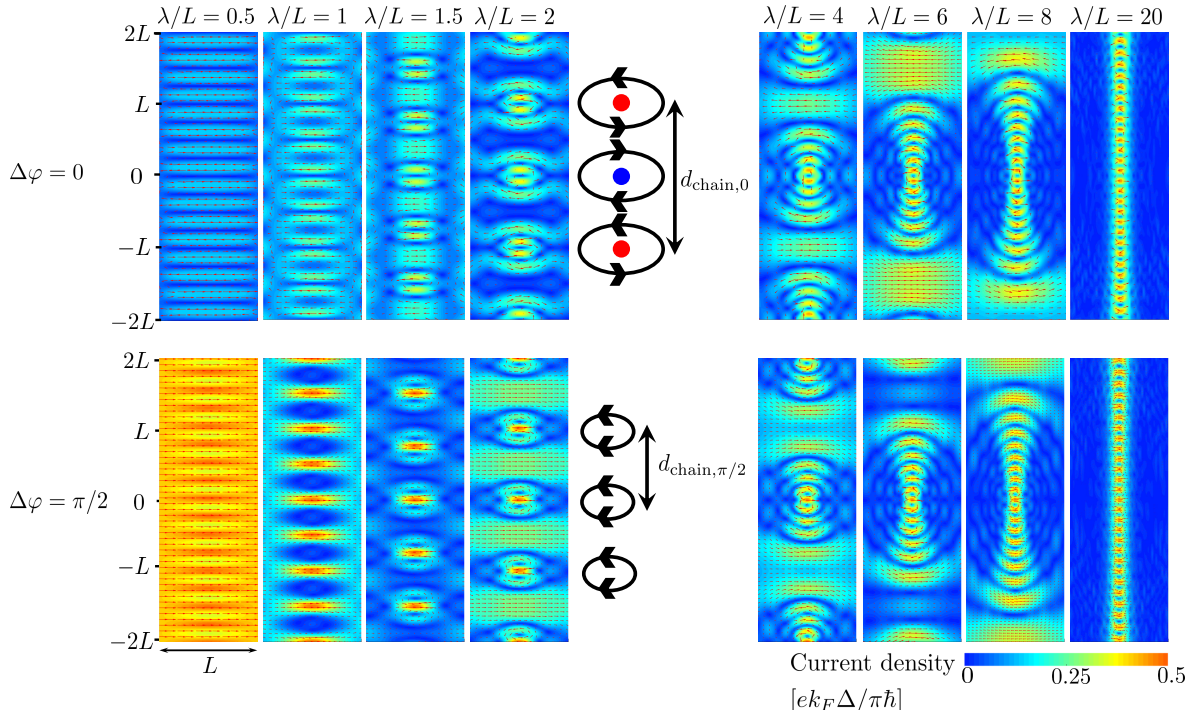

Figure 5.10: Scale plots of the supercurrent density in a magnetic field varying periodically with wavelength λ along the superconducting interface. The eight plot in the upper and lower row show the current density when the superconducting phase difference, $\Delta\varphi$, is zero and $\pi/2$, respectively. Chains (red) and anti-chains (blue) are indicated for the scale plot of wavelength $\lambda/L = 2$, along with the chain distance $d_{\text{chain}} = \lambda$. When $\Delta\varphi = \pi/2$ the chains and anti-chains are identical such that the chain distance is halved, $d_{\text{chain},\pi/2} = \lambda/2$. The current densities are calculated from equation (5.3), (5.12) and (5.47) at temperature $k_B T = \Delta$ and magnetic length $l_m/L = 0.3$.

smoothens out and approaches the constant critical current $I_{c,0}$ when the wavelength goes to zero, in correspondence with the limit found above.

Anti-symmetric field

We now let $\chi = 0$ in equation (5.44) such that the magnetic field is anti-symmetric about the x-axis with the phase shift

$$\gamma = -\frac{L^2}{l_m^2}\frac{\lambda}{\pi L}\frac{\sin\left(\frac{\pi L}{\lambda}\tan\theta_k\right)}{\frac{\pi L}{\lambda}\tan\theta_k}\sin\left(\frac{2\pi}{\lambda}\left[\left(y_0+\frac{\lambda}{4}\right)-x_0\tan\theta_k\right]\right) \tag{5.56}$$

This is equal to the symmetric field (5.47), only shifted by $\lambda/4$ along the y-axis. More general a phase χ in (5.44) give a pattern like we found for the symmetric field, only shifted by $\frac{\lambda}{2\pi}\left(\frac{\pi}{2}-\chi\right)$ along the interface. Hence we expect a similar, but shifted pattern as for the symmetric field. With $\chi = 0$ the first chain will be centered at $\lambda/4$ with a corresponding anti-chain centered at $-\lambda/4$. In fact for every chain centered at y_0 we expect to find an anti-chain centered at $-y_0$. Hence, the anti-

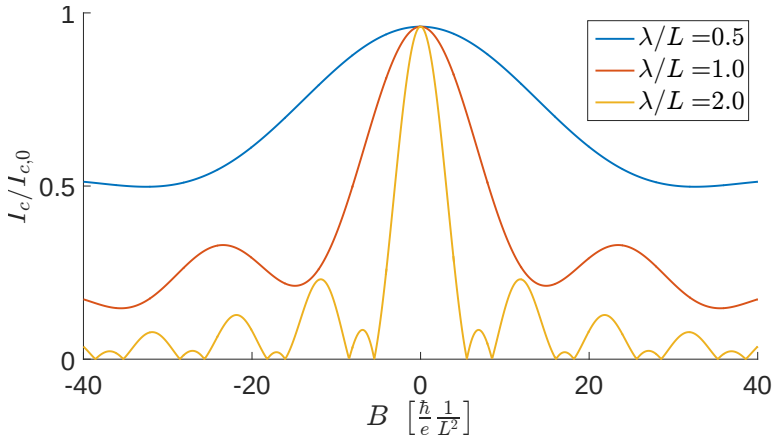

Figure 5.11: Plot of the critical current I_c versus the magnetic field strength B in a periodic field varying with three wavelengths, λ, along the superconducting interface in the normal region. The current is calculated numerically from equation (5.1), (5.12) and (5.47) at $\Delta\varphi = \pi/2$.

symmetric field generate an anti-symmetric pattern about the x-axis, unlike the symmetric field in which a chain centered at y_0 imply an identical chain centered at $-y_0$. Of course if the superconducting phase difference is $\Delta\varphi = 2\pi$, such that the current density is an even function of γ, the anti-chains turn into chains and also the anti-symmetric field reveals a symmetric pattern. These current densities, found from numerical calculations, are shown in figure (5.12).

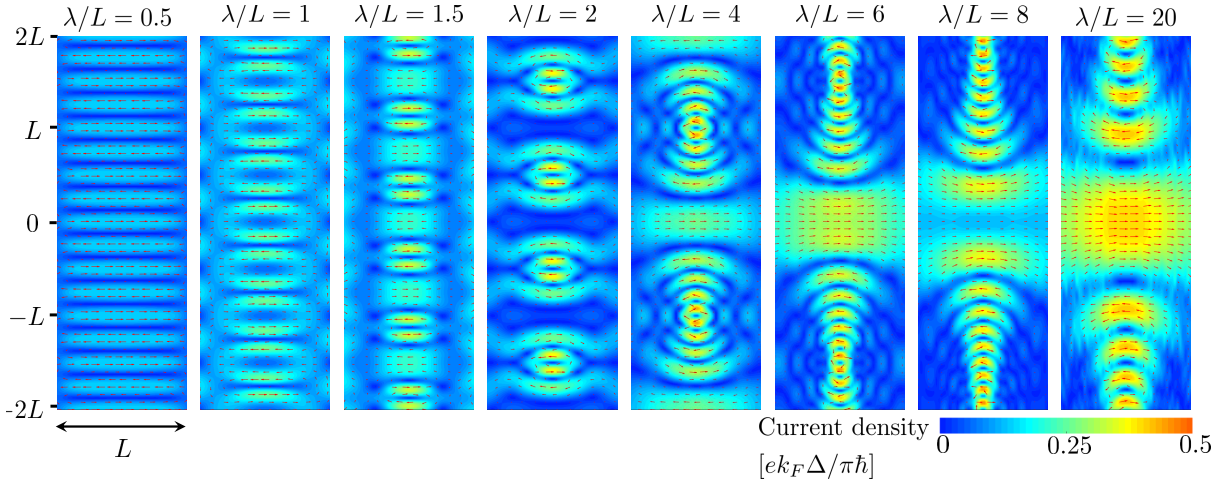

Figure 5.12: Scale plots of the supercurrent density in a magnetic field varying periodically with wavelength λ along the superconducting interface. The plots are the same as the upper row in figure 5.10 but shifted $\lambda/4$ along the interface due to a phase shift $\pi/2$ in the magnetic field. The current densities are calculated from equation (5.3), (5.12) and (5.56) at temperature $k_B T = \Delta$ and magnetic length $l_m/L = 0.3$.

Since the current density of the symmetric and anti-symmetric field along the interface only differ

by a shift of the center of the vortex rows along the y-axis, we expect the total current to be equal in the two cases, when $W \gg L$. This has also been confirmed numerically, and the critical current in the anti-symmetric field (or for any field of the form given in equation (5.44) for that matter) will be as shown in figure 5.11.

We have in this section found that with a field of the form in equation (5.44), varying periodically along the interface, we are able to control the pattern by changing the wavelength λ and the phase χ, as well as the superconducting phase difference $\Delta\varphi$ and the magnetic field strength B. This is a possibility we did not have in the uniform field in which we could control the vortex distance and size, but not the shape of the pattern. The fact that we can control in which areas of the junction the current is dominant using the modulation of the field is a new an interesting phenomenon. Not only will we be able to control the supercurrent, but as described in section 2.2 the presence of supercurrent will have direct consequence for the local density of states of single particles. Using the magnetic field we will thus be able to control in which areas *normal* current is allowed (as probed via e.g. an STM-tip). Controlling the supercurrent vortex pattern thus creates a tunable spatial map where normal tunneling currents are allowed or disallowed.

Chapter 6

Conclusion and outlook

In this thesis we have studied how the supercurrent density and the critical current in an SNS-junction is affected by an external magnetic field. The result found from a uniform magnetic field is already known [9, 10], however we have here considered modulated magnetic fields and seen how we are able to control the supercurrent via the field modulation. A key observation is that the supercurrent will be unaffected by the magnetic field for some modulations regardless of the field strength.

In chapter 4 we found the energy levels of the Andreev bound states which we in chapter 5 used to find the current density and critical current. We showed how the magnetic field accumulate a phase shift γ in the superconducting phase which depend on the field modulation and strength, as well as the trajectory of the electrons and holes, and thus give rise to quantum interference of the supercurrent. The modulations considered was a uniform field, a sinusoidal field varying along the junction and a sinusoidal field varying along the interfaces.

In the uniform field a chain of Josephson vortices appeared in the center of the junction along the interface and the critical current was found to be the familiar Fraunhofer oscillations, in accordance with earlier research [20–24, 28]. We found the same kind of vortex row in the symmetric sinusodial field varying along the junction. However, now the distance between the vortices could be controlled by changing the wavelength of the magnetic field and for some wavelengths we even found the current to be unaffected by the field. In the anti-symmetric field varying along the junction the Josephson vortices and Fraunhofer oscillations disappeared leaving a uniform current density. The wavelength of the magnetic field could be used to control the magnitude of the current and like the symmetric field some wavelengths left the supercurrent unaffected by the field. In the field varying along the interface the vortex row that was observed in the uniform field was repeated as rows and anti-rows in the center of the junction along the interfaces. Unlike the uniform field, we then found the current density pattern to depend on the superconducting phase difference, $\Delta\varphi$.

The analysis did in this thesis is based on several simplifications, such as transparent barriers at the superconducting interfaces and negligence of the Lorentz effect on the trajectories of the electrons and holes. In future work we may consider a more realizable system where we take into account barriers and the Lorentz force, as well as the modulated magnetic field, and in such analysis we expect the method considered in section 5.2 to be useful. Moreover, we have here only considered a circular Fermi surface. In a uniform field with warped Fermi surface, earlier research has shown the appearance of a 2D-pattern of Josephson vortices, unlike the single vortex chain we have seen here [28]. It would be interesting to also consider how non-uniform modulations of the magnetic field would affect the current for such Fermi surfaces. In this thesis we considered the effect originating from the vector potential of the magnetic field. However, the magnetic field will also effect the spin properties of the electrons and holes via the Zeeman-effect. It is reasonable to neglect the Zeeman-effect for the SNS-junction considered here as the effect from the vector potential will be much more dominant. However, if one replace the normal metal in the SNS-junction with a ferromagnet (SFS), the Zeeman-effect will be much more prominent, and it would be interesting to study how this affects the current in the junction [46]. Lastly, we have here considered s-wave superconductors with isotropic superconducting gap, and it would be interesting to instead consider the effect of magnetic field on a junction consisting of anisotropic d-wave superconductors, which to our knowledge has still not been explored.

Bibliography

[1] Dirk van Delft and Peter Kes. The discovery of superconductivity. 63(9):38–43, September 2010. ISSN 0031-9228, 1945-0699. URL http://physicstoday.scitation.org/doi/full/10.1063/1.3490499.

[2] W. Meissner and R. Ochsenfeld. Ein neuer effekt bei eintritt der supraleitfähigkeit. *Naturwissenschaften*, 21(44):787–788, 1933. ISSN 1432-1904. URL http://dx.doi.org/10.1007/BF01504252.

[3] A M Forrest. Meissner and ochsenfeld revisited. *European Journal of Physics*, 4(2):117, 1983. URL http://stacks.iop.org/0143-0807/4/i=2/a=011.

[4] J. Bardeen, L. N. Cooper, and J. R. Schrieffer. Theory of superconductivity. *Phys. Rev.*, 108:1175–1204, December 1957. URL http://link.aps.org/doi/10.1103/PhysRev.108.1175.

[5] R. D. Parks. *Superconductivity*. CRC Press, 1969. ISBN 978-0-8247-1521-2.

[6] B. Pannetier and H. Courtois. Andreev reflection and proximity effect. *Journal of Low Temperature Physics*, 118(5):599–615, 2000. ISSN 1573-7357. URL http://dx.doi.org/10.1023/A:1004635226825.

[7] Linder Jacob and Robinson Jason W. A. Superconducting spintronics. *Nat Phys*, 11(4):307–315, apr 2015. ISSN 1745-2473. doi: http://dx.doi.org/10.1038/nphys324210.1038/nphys3242.

[8] JM Rowell. Magnetic field dependence of the josephson tunnel current. *Physical Review Letters*, 11(5):200, 1963. URL http://journals.aps.org/prl/abstract/10.1103/PhysRevLett.11.200.

[9] Michael Tinkham. *Introduction to Superconductivity*. Courier Corporation, 1996. ISBN 978-0-486-13472-7.

[10] Antonio Barone and Gianfranco Paternò. *Physics and applications of the Josephson effect*. Wiley, 1982. ISBN 978-0-471-01469-0.

[11] Jarillo-Herrero P. Oostinga J. B. Vandersypen L. M. K. Heersche, H. B. and A. F. Morpurgo. Bipolar supercurrent in graphene. *Nature*, 446:56–59, 2007. ISSN 0028-0836. URL http://dx.doi.org/10.1038/nature05555.

[12] CaladoV. E., GoswamiS., NandaG., DiezM., AkhmerovA. R., WatanabeK., TaniguchiT., KlapwijkT. M., and VandersypenL. M. K. Ballistic Josephson junctions in edge-contacted graphene. *Nat Nano*, 10(9):761–764, September 2015. ISSN 1748-3387. URL http://dx.doi.org/10.1038/nnano.2015.156.

[13] M. T. Allen, O. Shtanko, I. C. Fulga, J. I. J. Wang, D. Nurgaliev, K. Watanabe, T. Taniguchi, A. R. Akhmerov, P. Jarillo-Herrero, L. S. Levitov, and A. Yacoby. Visualization of phase-coherent electron interference in a ballistic graphene josephson junction, 2015. URL https://arxiv.org/abs/1506.06734.

[14] Zhu-M. J. Fal'ko V. I. Mishchenko A. Kretinin A. V. Novoselov K. S. Woods C. R. Watanabe K. Taniguchi T. Geim A. K. Ben Shalom, M. and J. R. Prance. Quantum oscillations of the critical current and high-field superconducting proximity in ballistic graphene. *Nat Phys*, 12(4):318–322, April 2016. ISSN 1745-2473. URL http://dx.doi.org/10.1038/nphys3592.

[15] M. Veldhorst, M. Snelder, M. Hoek, T. Gang, V. K. Guduru, X. L. Wang, U. Zeitler, W. G. van der Wiel, A. A. Golubov, H. Hilgenkamp, and A. Brinkman. Josephson supercurrent through a topological insulator surface state. *Nat Mater*, 11(5):417–421, May 2012. ISSN 1476-1122. URL http://dx.doi.org/10.1038/nmat3255.

[16] J. R. Williams, A. J. Bestwick, P. Gallagher, Seung Sae Hong, Y. Cui, Andrew S. Bleich, J. G. Analytis, I. R. Fisher, and D. Goldhaber-Gordon. Unconventional josephson effect in hybrid superconductor-topological insulator devices. *Phys. Rev. Lett.*, 109:056803, Jul 2012. URL http://link.aps.org/doi/10.1103/PhysRevLett.109.056803.

[17] Sean Hart, Hechen Ren, Timo Wagner, Philipp Leubner, Mathias Muhlbauer, Christoph Brune, Hartmut Buhmann, Laurens W. Molenkamp, and Amir Yacoby. Induced superconductivity in the quantum spin Hall edge. *Nat Phys*, 10(9):638–643, September 2014. ISSN 1745-2473. URL http://dx.doi.org/10.1038/nphys3036.

[18] Vlad S. Pribiag, BeukmanArjan J. A., Fanming Qu, Maja C. Cassidy, Christophe Charpentier, Werner Wegscheider, and Leo P. Kouwenhoven. Edge-mode superconductivity in a two-dimensional topological insulator. *Nat Nano*, 10(7):593–597, July 2015. ISSN 1748-3387. URL http://dx.doi.org/10.1038/nnano.2015.86.

[19] A.A. Abrikosov. The magnetic properties of superconducting alloys. *Journal of Physics and Chemistry of Solids*, 2(3):199–208, 1957. ISSN 0022-3697. URL http://www.sciencedirect.com/science/article/pii/0022369757900835.

[20] J. C. Cuevas and F. S. Bergeret. Magnetic interference patterns and vortices in diffusive sns junctions. 2007. URL http://journals.aps.org/prl/abstract/10.1103/PhysRevLett.99.217002.

[21] F. S. Bergeret and J. C. Cuevas. The Vortex State and Josephson Critical Current of a Diffusive SNS Junction. *Journal of Low Temperature Physics*, 153(5):304–324, 2008. ISSN 1573-7357. doi: 10.1007/s10909-008-9826-2. URL http://dx.doi.org/10.1007/s10909-008-9826-2.

[22] Mohammad Alidoust, Granville Sewell, and Jacob Linder. Non-fraunhofer interference pattern in inhomogeneous ferromagnetic josephson junctions. *Phys. Rev. Lett.*, 108:037001, Jan 2012. URL http://link.aps.org/doi/10.1103/PhysRevLett.108.037001.

[23] Mohammad Alidoust and Klaus Halterman. Proximity induced vortices and long-range triplet supercurrents in ferromagnetic josephson junctions and spin valves. 2015. URL http://aip.scitation.org/doi/full/10.1063/1.4908287.

[24] Morten Amundsen and Jacob Linder. General solution of 2d and 3d superconducting quasiclassical systems: coalescing vortices and nanoisland geometries. Mar 2015. URL https://www.ncbi.nlm.nih.gov/pmc/articles/PMC4785343/.

[25] J. P. Heida, B. J. van Wees, T. M. Klapwijk, and G. Borghs. Nonlocal supercurrent in mesoscopic josephson junctions. *Phys. Rev. B*, 57:R5618–R5621, Mar 1998. URL http://link.aps.org/doi/10.1103/PhysRevB.57.R5618.

[26] Victor Barzykin and Alexandre M. Zagoskin. Coherent transport and nonlocality in mesoscopic SNS junctions: anomalous magnetic interference patterns. *Superlattices and Microstructures*, 25(5):797 – 807, 1999. ISSN 0749-6036. doi: http://dx.doi.org/10.1006/spmi.1999.0731. URL http://www.sciencedirect.com/science/article/pii/S0749603699907310.

[27] Minsoo Kim, Dongchan Jeong, Gil-Ho Lee, Yun-Sok Shin, Hyun-Woo Lee, and Hu-Jong Lee. Tuning Locality of Pair Coherence in Graphene-based Andreev Interferometers. *Scientific Reports*, 5:8715, March 2015. URL http://dx.doi.org/10.1038/srep08715.

[28] V. P. Ostroukh, B. Baxevanis, A. R. Akhmerov, and C. W. J. Beenakker. Two-dimensional josephson vortex lattice and anomalously slow decay of the fraunhofer oscillations in a ballistic sns junction with a warped fermi surface. *Phys. Rev. B*, 94:094514, Sep 2016. URL http://link.aps.org/doi/10.1103/PhysRevB.94.094514.

[29] Hendrik Meier, Vladimir I. Fal'ko, and Leonid I. Glazman. Edge effects in the magnetic interference pattern of a ballistic sns junction. *Phys. Rev. B*, 93:184506, May 2016. URL http://link.aps.org/doi/10.1103/PhysRevB.93.184506.

[30] F. London and H. London. The electromagnetic equations of the supraconductor. *Proceedings of the Royal Society of London A: Mathematical, Physical and Engineering Sciences*, 149(866): 71–88, 1935. ISSN 0080-4630. URL http://rspa.royalsocietypublishing.org/content/149/866/71.

[31] K. Fossheim and A. Sudbø. *Superconductivity: Physics and Applications*. Wiley, Chichester, West Sussex, 2004. ISBN 9780470844526.

[32] P. G. de Gennes. Boundary effects in superconductors. *Rev. Mod. Phys.*, 36:225–237, Jan 1964. URL http://link.aps.org/doi/10.1103/RevModPhys.36.225.

[33] G. E. Blonder, M. Tinkham, and T. M. Klapwijk. Transition from metallic to tunneling regimes in superconducting microconstrictions: Excess current, charge imbalance, and supercurrent conversion. *Phys. Rev. B*, 25:4515–4532, Apr 1982. URL http://link.aps.org/doi/10.1103/PhysRevB.25.4515.

[34] A. F. Andreev. The thermal conductivity of the intermediate state in superconductors. *Sov. Phys. JETP*, 19:1228 – 1231, Nov 1964. URL http://www.jetp.ac.ru/cgi-bin/e/index/e/19/5/p1228?a=list.

[35] H. A. Blom, A. Kadigrobov, A. M. Zagoskin, R. I. Shekhter, and M. Jonson. Dissipative electron transport through andreev interferometers. *Phys. Rev. B*, 57:9995–10016, Apr 1998. URL http://link.aps.org/doi/10.1103/PhysRevB.57.9995.

[36] P. A. M. Benistant, H. van Kempen, and P. Wyder. Direct observation of andreev reflection. *Phys. Rev. Lett.*, 51:817–820, Aug 1983. URL http://link.aps.org/doi/10.1103/PhysRevLett.51.817.

[37] B. D. Josephson. Possible new effects in superconductive tunnelling. *Physics Letters*, 1(7):251 – 253, 1962. ISSN 0031-9163. URL http://www.sciencedirect.com/science/article/pii/0031916362913690.

[38] Meng Xiang-Guo, Wang Ji-Suo, and Liang Bao-Long. Cooper-Pair Number-Phase Quantization for Inductance Coupling Circuit Including Josephson Junctions. *Chinese Physics Letters*, 25(4):1419, 2008. URL http://stacks.iop.org/0256-307X/25/i=4/a=069.

[39] A. A. Golubov, M. Yu. Kupriyanov, and E. Il'ichev. The current-phase relation in josephson junctions. *Rev. Mod. Phys.*, 76:411–469, Apr 2004. URL http://link.aps.org/doi/10.1103/RevModPhys.76.411.

[40] SHINYA Hasuo and Takeshi Imamura. Digital logic circuits. *Proceedings of the IEEE*, 77(8): 1177–1193, 1989. URL http://ieeexplore.ieee.org/document/34118/.

[41] R. Kleiner and P. Müller. Intrinsic josephson effects in high-t_c superconductors. *Phys. Rev. B*, 49:1327–1341, Jan 1994. URL http://link.aps.org/doi/10.1103/PhysRevB.49.1327.

[42] Yakov I. Granovskii. Sommerfeld formula and Dirac's theory. *Physics-Uspekhi*, 47(5):523, 2004. URL http://stacks.iop.org/1063-7869/47/i=5/a=L06.

[43] C. W. J. Beenakker. Universal limit of critical-current fluctuations in mesoscopic josephson junctions. *Phys. Rev. Lett.*, 67:3836–3839, Dec 1991. URL http://link.aps.org/doi/10.1103/PhysRevLett.67.3836.

[44] IO Kulik. Macroscopic quantization and the proximity effect in sns junctions. *Soviet Journal of Experimental and Theoretical Physics*, 30:944, 1969. URL http://www.jetp.ac.ru/cgi-bin/e/index/e/30/5/p944?a=list.

[45] Y. Aharonov and D. Bohm. Significance of electromagnetic potentials in the quantum theory. *Phys. Rev.*, 115:485–491, Aug 1959. URL http://link.aps.org/doi/10.1103/PhysRev.115.485.

[46] A. I. Buzdin. Proximity effects in superconductor-ferromagnet heterostructures. *Rev. Mod. Phys.*, 77:935–976, Sep 2005. URL http://link.aps.org/doi/10.1103/RevModPhys.77.935.